



City Research Online

City, University of London Institutional Repository

Citation: Pelletier, J. D., Sherman, D. J., Ellis, J. T., Farrell, E. J., Jackson, N. L., Li, B. Y., Nordstrom, K. F., Maia, L. P. & Omidyeganeh, M. (2015). Dynamics of sediment storage and release on aeolian dune slip faces: A field study in Jericoacoara, Brazil. *Journal of Geophysical Research: Earth Surface*, 120(9), pp. 1911-1934. doi: 10.1002/2015jf003636

This is the published version of the paper.

This version of the publication may differ from the final published version.

Permanent repository link: <https://openaccess.city.ac.uk/id/eprint/12538/>

Link to published version: <https://doi.org/10.1002/2015jf003636>

Copyright: City Research Online aims to make research outputs of City, University of London available to a wider audience. Copyright and Moral Rights remain with the author(s) and/or copyright holders. URLs from City Research Online may be freely distributed and linked to.

Reuse: Copies of full items can be used for personal research or study, educational, or not-for-profit purposes without prior permission or charge. Provided that the authors, title and full bibliographic details are credited, a hyperlink and/or URL is given for the original metadata page and the content is not changed in any way.

City Research Online:

<http://openaccess.city.ac.uk/>

publications@city.ac.uk

RESEARCH ARTICLE

10.1002/2015JF003636

Key Points:

- Barchan slip faces exhibit complex variations in grain-flow activity
- The critical angle depends on wind speed, sand moisture, and slip-face height
- Diurnal variations in wind speed drive diurnal cycles of grain-flow activity

Correspondence to:

J. D. Pelletier,
jdpellet@email.arizona.edu

Citation:

Pelletier, J. D., D. J. Sherman, J. T. Ellis, E. J. Farrell, N. L. Jackson, B. Li, K. F. Nordstrom, L. P. Maia, and M. Omidyeganeh (2015), Dynamics of sediment storage and release on aeolian dune slip faces: A field study in Jericoacoara, Brazil, *J. Geophys. Res. Earth Surf.*, 120, 1911–1934, doi:10.1002/2015JF003636.

Received 8 JUN 2015

Accepted 26 AUG 2015

Accepted article online 29 AUG 2015

Published online 25 SEP 2015

Dynamics of sediment storage and release on aeolian dune slip faces: A field study in Jericoacoara, Brazil

Jon D. Pelletier¹, Douglas J. Sherman², Jean T. Ellis³, Eugene J. Farrell⁴, Nancy L. Jackson⁵, Bailiang Li⁶, Karl F. Nordstrom⁷, Luis Parente Maia⁸, and Mohammad Omidyeganeh⁹

¹Department of Geosciences, University of Arizona, Tucson, Arizona, USA, ²Department of Geography, University of Alabama, Tuscaloosa, Alabama, USA, ³Department of Geography and Marine Science Program, University of South Carolina, Columbia, South Carolina, USA, ⁴School of Geography and Archeology, National University of Ireland, Galway, Ireland, ⁵Department of Chemistry and Environmental Science, New Jersey Institute of Technology, Newark, New Jersey, USA, ⁶Department of Environmental Science, Xi'an Jiaotong-Liverpool University, Suzhou, China, ⁷Department of Marine and Coastal Sciences, Rutgers University, New Brunswick, New Jersey, USA, ⁸Instituto do Ciências do Mar, Universidade Federal do Ceará, Fortaleza, Brazil, ⁹School of Mathematics, Computer Science and Engineering, City University London, London, UK

Abstract Sediment transport on the lee sides of aeolian dunes involves a combination of grain-fall deposition on the upper portion of the slip face until a critical angle is exceeded, transport of a portion of those sediments down the slip face by grain flows and, finally, deposition at an angle of repose. We measured the mean critical and repose angles and the rate of slip-face avalanching using terrestrial laser scanning (TLS) on two barchans of different size in Jericoacoara, Brazil. Wind speeds and sand fluxes were measured simultaneously at the dune crests. We found that the mean critical decreased with increasing wind speed. We attribute this effect to turbulent shear stresses, the magnitude of which we quantified using 3-D large eddy simulation modeling, that randomly act down the slip face (i.e., in the direction of gravity) to trigger grain flows at lower angles than would be possible with gravity stresses alone. We developed and tested a new predictive model for the frequency of avalanching that depends on both the sediment flux delivered to the slip face and changes in the critical angle with time. In this model, increasing turbulent shear stresses drive avalanching even in the absence of sand flux delivered to the slip face if the critical angle decreases below the slope angle. We also document that the mean critical angle decreases slightly with increasing slip-face height. These results have important implications for aeolian dune evolution, interpretations of aeolian stratigraphy, and granular mechanics.

1. Introduction

1.1. Problem Statement

The physics of dunes, dune evolution (characteristic landform scale and morphologies), and the storage time and cycling of sediments through landforms remain fundamental research questions in geomorphology [Lancaster *et al.*, 1996; Wiggs *et al.*, 1996; Hesp and Hastings, 1998; Andreotti *et al.*, 2002; Hersen *et al.*, 2002; Elbelrhiti *et al.*, 2005; Claudin and Andreotti, 2006; Fischer *et al.*, 2008; Katsuki *et al.*, 2011; Zhang *et al.*, 2014] and planetary science [Bourke *et al.*, 2008; Bourke, 2010; Horgan and Bell, 2012; Warren, 2013]. The migration of aeolian dunes involves the entrainment and transport of sand up the stoss side and grain-fall deposition and grain-flow avalanching down the lee-side slip face [Bagnold, 1941; Allen, 1970; Hunter, 1985]. Despite the important role that lee-side sediment-transport processes have on dune evolution and migration, the majority of dune-evolution studies focus on the processes of sediment transport up the stoss slope. Landscape evolution models of aeolian dunes, in particular, have generally assumed that the dune slip face maintains a constant angle such that any sediment flux coming over the brinkline is immediately transported down the slip face [e.g., Werner, 1995; Andreotti *et al.*, 2002; Baas and Nield, 2007; Shao, 2008; Pelletier, 2009; Zhang *et al.*, 2010]. This assumption may be appropriate for understanding dune evolution over time scales of weeks to years, but it simplifies a rich and complex dynamical process over time scales of seconds to days.

Some of the complexity associated with slip-face evolution derives from the fact that the kinematics of granular materials are governed by two angles: a critical angle of stability, or critical angle for short, to which a portion of the slip face must steepen before a grain flow is triggered, and an (lower) angle of repose at

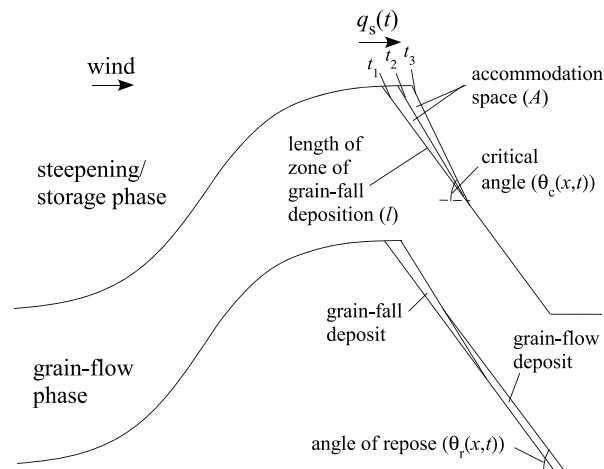


Figure 1. Schematic cross-sectional diagram of storage-and-release dynamics associated with dune slip-face evolution. In the steepening/storage phase, grainfall deposits accumulate on the upper portion of the slip face until a critical angle, θ_c , is reached, at which point a grain flow is triggered. In the grain-flow phase, a portion of the grain-fall deposit is advected down the slope and deposited at the angle of repose, θ_r , that is lower than θ_c . The periodicity of cycles of storage and release is hypothesized to depend on the difference between the critical angle and the angle of repose (defined herein as the relaxation angle), as well as on the sediment flux over the brinkline, q_s . In addition, we hypothesize that a decrease in θ_c with time can trigger grainflow activity independent of q_s .

that extends the full length of the slope, grain flows may only traverse a portion of the slope length [McDonald and Anderson, 1996; Breton *et al.*, 2008].

Previous studies of grain-flow avalanching used video recordings to measure the frequency and spatial extent of avalanches. Breton *et al.* [2008], for example, used video data to establish that the frequency of grain flows on a dune in the Namib depends on wind speed and sand transport rate. These authors also documented that flow area is inversely proportional to the interval between flows and thus also depends on wind speed and sand transport rates. Sutton *et al.* [2013a, 2013b] conducted a series of elegant laboratory experiments demonstrating the evolution of a 1.2 m tall slip face, taking advantage of recent technological developments in high-resolution topographic surveying with laser scanning. They found that the frequency of grain-flow avalanches was a function of sediment flux over the brinkline. Sutton *et al.* [2013a, 2013b] measured a mean critical angle of 34° and a mean angle of repose of 32° .

The results of Sutton *et al.* [2013a, 2013b] are broadly consistent with the conceptual “storage-and-release” model illustrated in Figure 1. In this model, the frequency of grain flows is proportional to the sediment flux coming over the brinkline because that flux determines how fast the accommodation space created by a previous grain flow can be filled up before another grain flow is triggered. The goal of this study is to further test and develop the conceptual framework of storage-and-release dynamics of dune slip faces developed by Breton *et al.* [2008], Sutton *et al.* [2013a, 2013b], and the classic works of Bagnold [1941], Allen [1970], Hunter [1985], Anderson [1988], and McDonald and Anderson [1996].

In this paper we document that significant variations in the mean critical angle and mean angle of repose occur as a function of time in dune slip faces and that such variations control the frequency of avalanching. Our hypothesis is that the diurnal variations in the mean critical angle are driven by diurnal variations in the magnitudes of turbulent shear stresses that act randomly on the slip face and, when they are temporarily directed downslope (in the direction of gravity), can trigger avalanches at lower slope angles than would otherwise be possible. We show that the maximum frequency of avalanching occurs significantly earlier each day than the time of maximum sediment flux coming over the brinkline. As such, there must be some additional control on the frequency of avalanching in addition to the standard model of storage-and-release of grain-fall deposits in which the frequency of avalanching is proportional to the sediment flux coming over the brinkline.

which grain-flow deposits settle (Figure 1) [e.g., Brown and Richards, 1966; Quartier *et al.*, 2000]. The difference between these two angles is defined as the relaxation angle [Duran, 2000]. The factors that control these angles are not fully understood. The relaxation angle has been reported to be approximately 2° [Duran, 2000]. However, relaxation angles measured in the laboratory vary from less than 1° [Bagnold, 1966] to as high as 5° [Börzsönyi *et al.*, 2008]. Neither the critical angle nor the angle of repose should be considered uniform in space or constant in time. The critical angle, which depends on the static friction angle, is likely to vary spatially as a consequence of variations in grain shape (i.e., roundedness) and compaction [Bareither *et al.*, 2008] and perhaps also as a function of time due to dynamic stresses acting on the surface (e.g., wind flow). Note that while Figure 1 shows an example grain flow

Dune slip faces are worthy of study in part because they have failure mechanisms that are broadly similar to those of more general (i.e., cohesive) hillslopes. Because slip faces typically lack the heterogeneity of variable soil moisture, root strength, etc., studying mass movements on slip faces has the potential to inform our understanding of mass movements on hillslopes through a better understanding of how mass movements work in the relative absence of heterogeneity. Another reason to study dune slip faces is that they are an exemplar of “sticky” geomorphic systems [Jerolmack, 2008]. Many geomorphic systems (and indeed many geologic systems) are governed by storage-and-release dynamics in which the crossing of a threshold induces a positive feedback that tends to allow activity to persist once initiated. In the case of dune slip faces, flow initiation reduces intergranular friction and thereby promotes faster flow in a positive feedback (with event sizes ultimately limited by the size of the slip face). The deposition of sediments at the base of a slip face creates accommodation space for the storage of sediment at the top, potentially setting up a bistable or quasiperiodic behavior. Geologic faults have complex internal dynamics that result from the differences between static and kinetic coefficients of friction [e.g., Pelletier, 2000]. Such a difference in friction allows faults to have both bistable and chaotic behavior [e.g., Huang and Turcotte, 1990]. Active fluvial channels on deltas and alluvial fans exhibit autogenic cyclicity in which local aggradation occurs until a critical elevation is achieved, after which channels avulse to a new location, prograde, then backfill until the threshold of avulsion recurs [Reitz and Jerolmack, 2012] (W. E. Weaver, Experimental study of alluvial fans, unpublished PhD dissertation, 423 pp., Colorado State University, Fort Collins, Colorado, 1984). Sticky systems are important to understand in part because their complex autogenic dynamics have the potential to “shred” environmental signals, i.e., to produce a complex output even in the case of simple (e.g., constant) inputs [Jerolmack and Paola, 2010]. By comparing and contrasting threshold-dominated or sticky systems across different process domains, we have the potential to learn more about how they behave as a class of systems. Finally, grain flows are the primary aeolian deposit type preserved in the stratigraphic record [Hunter, 1977]. As such, studying grain-flow dynamics has the potential to inform our interpretation of aeolian sediments preserved in ancient sequences.

1.2. Study Site

Field measurements were conducted on 4–9 November 2013 in the Jericoacoara dune field, Ceará, Brazil (Figure 2a). This location was chosen because of the range of sizes of barchan slip faces (with some up to 30 m tall) and the strong and consistent winds that occur at this time of year [Jimenez et al., 1999]. The timing of the fastest wind speeds ($u > 10 \text{ m s}^{-1}$) coincides with the occurrence of the highest air temperatures (approximately 30°C) to provide near-neutral conditions in the boundary layer. The Jericoacoara dune field is the site of many studies of aeolian geomorphological processes, including fundamental studies of aeolian transport [Sauermaun et al., 2003; Ellis et al., 2012; Li et al., 2010, 2014; Farrell et al., 2012; Sherman et al., 2013a, 2013b] and studies of the behavior of barchans and their evolution [e.g., Hesp, 2004; Herrmann et al., 2005; Maia et al., 2005; Parteli et al., 2007; Levin et al., 2009; Wu et al., 2011].

Barchan migration rates exceeding 0.1 m d^{-1} are common in the 5 month period of August to December in the Jericoacoara dune field. Wind speeds exceed the threshold for saltation almost every afternoon during these months, and there is minimal rainfall, averaging 123 mm over the same period (measured at Fortaleza (240 km to the ESE) [Jimenez et al., 1999]). Winds in the study area have a large diurnal cycle. Figure 3 plots wind directions measured at Parnaíba airport (located 130 km to the west of Jericoacoara along a relatively straight section of coastline) and wind speeds we measured on the smaller of the two dunes we studied. Wind speed is a minimum in the early morning (approximately 03:00, where c. (circa) represents approximate time henceforth) and increases most quickly between 10:00 and 12:00, reaching a maximum in the early afternoon (approximately 12:00–14:00). As the winds speed up in the morning they also rotate counterclockwise from ESE (early morning) to the predominant dune-migration direction of ENE (late morning and afternoon). This shift in wind direction is significant for evaluating alternative hypotheses for the factors controlling temporal variations in the mean critical angle, a point to which we return in section 3. Diurnal cyclicity in wind speed and/or sand transport is common in land areas globally [e.g., Dai and Deser, 1999; Stout, 2010]. As such, to the extent that diurnal cyclicity controls slip-face evolution in Jericoacoara, it can be expected to be important in other dune fields as well.

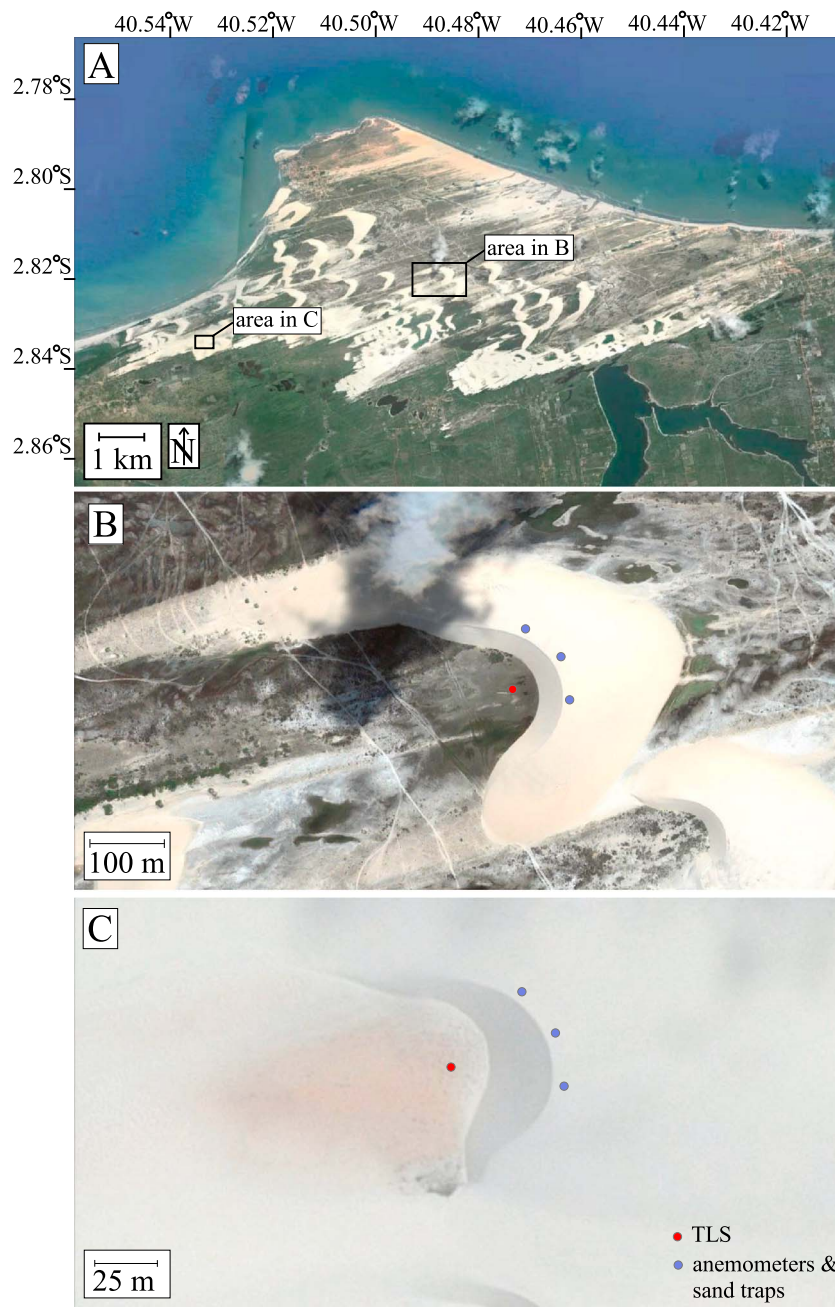


Figure 2. Aerial photographs of the study site: (a) the Jericoacoara dune field, (b) the larger of the two dunes in the study, and (c) the smaller of the two dunes. The locations of the TLS (red dots) and anemometers and sand traps (blue dots) are also shown. Image source:

2. Methods

2.1. Wind Speed, Sand Flux, and Grain-Diameter Measurements and Postprocessing

We measured wind speeds at 0.75 m above the ground at three locations just upwind of the brinkline (Figure 2). Wind speeds were measured continuously at 1 Hz from 08:00 to 16:00 each day and at 0.1 Hz for continuous 24 h periods. We also measured sand flux at intervals of 20 or 25 min and sampled for durations of one to 5 min using two or three vertically stacked, 0.1×0.1 m hose-style sand traps [Sherman *et al.*, 2014] placed

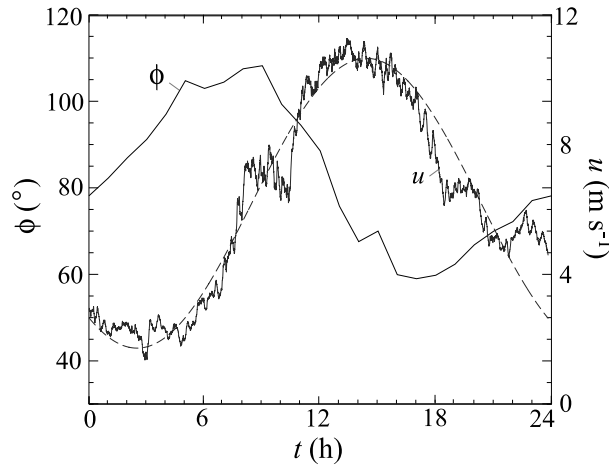


Figure 3. Average hourly wind direction (ϕ) at Parnaíba airport (located 130 km west of Jericoacoara) during November (period of record: 1943–2013), and 5 min average wind speed (u) measured 0.75 m above the ground at the crest of the small dune on 8 November 2013. The dashed line is a sinusoidal fit to the wind speed (see section 3 for further discussion).

rainfall event during the early morning of 4 November, we also obtained a bulk sand sample for weighing, drying, and reweighing to estimate moisture content by per cent weight.

Shear velocities, u_* , at the dune crests were estimated using the wind-speed data and the “law of the wall”:

$$u(z) = \frac{u_*}{\kappa} \ln\left(\frac{z}{z_0}\right). \tag{1}$$

where κ is the von Kármán constant (0.41). The aerodynamic roughness length, z_0 , is a function of shear velocity [Sherman, 1992; Sherman and Farrell, 2008]; hence, we used equation (1) iteratively; i.e., we computed an estimate of u_* using each instantaneous wind speed, together with an initial z_0 value of $d_{50}/15$ and used the modified-Charnock relation of Sherman [1992] and Sherman and Farrell [2008]:

$$z_0 = \frac{d_{50}}{15} + C_m \frac{(u_* - u_{*t})^2}{g}, \tag{2}$$

to obtain refined estimates of z_0 for every u_* value, where d_{50} and u_{*t} represent the median grain diameter and threshold shear velocity parameters, respectively, and $C_m = 0.132$ (the average value that Sherman and Farrell [2008] obtained for field conditions). This procedure was repeated until convergence, i.e., until each u_* value varied by less than 0.1% between iterations.

2.2. Terrestrial Laser Scanning Data Collection and Postprocessing

A Leica C10 scanner located downwind of the slip face along the dune centerline was used to acquire terrestrial laser scanning (TLS) data from a fixed location downwind of each slip face from approximately 09:00–16:00 each day. The slip face of the larger barchan was scanned approximately every 13 min, while that of the smaller dune was scanned approximately every 7 min. The Leica C10 has an inherent surface-model accuracy of 2 mm under ideal conditions (i.e., scanning a vegetation-free surface during slow winds) [Hodge et al., 2009] at the instrument-to-target distances of this study, i.e., 20–100 m. We adopted a threshold for change detection equal to 5 mm for this study because we found that this value effectively excludes errors in the data resulting from wind gusts that occasionally buffeted the instrument. Scans obtained on a particular day were automatically in the same coordinate system because the scanner was not moved during the day. To absolutely georeference each point cloud and to allow accurate change detection from 1 day to the next (which necessarily involves minor displacement of the scanner location between daily deployments), we scanned three Leica disk targets that were kept in fixed locations for the duration of the field campaign. The locations of these targets were surveyed with a Real-Time Kinematic Global Positioning System to obtain absolute georeferencing.

1 m from the anemometers. The trapped sand was weighed, and the results were converted to $\text{g m}^{-1} \text{s}^{-1}$ (for unit mass flux) and $\text{m}^2 \text{s}^{-1}$ (for unit volumetric flux), assuming a bulk density of 1500 kg m^{-3} (porosity of 43%) for the latter (“unit” indicates flux per unit width in the direction perpendicular to transport). We use q_s to denote the unit mass flux of sand and q_v to denote the unit volumetric flux of sand. A volumetric measure of unit sediment flux is needed to relate the sediment flux coming over the brinkline to the frequency of avalanching. The particle-size distributions of a subset of the trapped sand samples were measured using a Mastersizer 2000 laser-diffraction particle-size analyzer. Because of a

Each point cloud was filtered to remove points representing personnel, instruments, and interdune areas, in order to produce point clouds that included only the slip face. Each filtered point cloud has a mean point spacing of approximately 10 mm on the large dune and 5 mm on the small dune. A triangulated irregular network (TIN) was constructed for each point cloud, and each TIN was interpolated to create a raster with point spacing of 0.02 m on the large dune and 0.01 m on the small dune. The rasters from successive scans were then differenced to create digital elevation models (DEMs) of Difference (DoDs) that represent the topographic change that occurred during the time intervals between successive scans. This point cloud, TIN, raster approach is standard in multitemporal lidar change detection [e.g., *Wheaton et al.*, 2010]. We used a raster-based change-detection methodology (as opposed to differencing point clouds directly) based on our familiarity with this approach, the need to efficiently process hundreds of scans, and because the relatively simple shape of our slip faces results in a relatively uniform and high density of points appropriate for raster-based techniques.

Maps of topographic gradient or slope were constructed from each DEM using a centered difference:

$$|\vec{\nabla} z| = \sqrt{\left(\frac{z_{i+1,j} - z_{i-1,j}}{2\Delta x}\right)^2 + \left(\frac{z_{i,j+1} - z_{i,j-1}}{2\Delta y}\right)^2} \quad (3)$$

where z is the local elevation and x and y are the distance along each Cartesian direction, and i and j are pixel indices. Measurements of the mean critical angle through time were obtained by averaging the slopes of each pixel from portions of the slip face that underwent erosion between consecutive scans. Similarly, measurements of the mean angle of repose were made by averaging the slopes of portions of the slip face that underwent deposition between consecutive scans.

Given a map of topographic change, it is possible to numerically integrate elevation changes along transport pathways to obtain a map of sediment flux. The Exner equation [*Exner*, 1925], expressed in a finite difference, volumetric form, states

$$\frac{\Delta z_i}{\Delta t} = -\frac{1}{1-\lambda} \frac{\Delta q_v}{\Delta s}, \quad (4)$$

where Δz_i is the change in ground-surface elevation over a time interval Δt , λ is the sediment porosity (assumed here to be 0.43 based on a bulk density of 1500 kg m^{-3} and a grain density of 2650 kg m^{-3}), q_v is the unit volumetric sediment flux, and Δs is the distance between sample points in the direction of steepest descent (assumed to be the direction of grain-flow transport). Equation (4) shows that given values for the erosion/deposition rate, i.e., $\Delta z_i/\Delta t$, along a profile, the unit volumetric sediment flux can be determined via Euler integration along the profile.

$$q_v = -(1-\lambda) \sum_{i=1}^n \frac{\Delta z_i}{\Delta t} \Delta s + q_0 \quad (5)$$

where n is the number of points along the profile. The constant of integration q_0 is constrained in this case by assuming q_v is zero at the base of the slip face.

The DoDs were also used to measure the frequency of avalanching. The frequency of avalanching was quantified as the fraction of the surveyed slip-face area that underwent erosion or deposition during the time interval between scans divided by the duration of the interval. For example, a frequency of avalanching of 1 h^{-1} means that erosion or deposition occurs over the entire slip face, on average, once per hour.

2.3. Computational Fluid Dynamics Modeling and Slope Stability Analysis

To demonstrate that the diurnal variations in the mean critical angle are driven by diurnal variations in turbulent shear stresses, we analyzed the output of a 3-D large eddy simulation (LES) model of turbulent flow over a barchan at a flow Reynolds number $Re \approx 26,000$ reported by *Omidyeganeh et al.* [2013]. This model predicts the means and standard deviations of turbulent shear stresses acting on different segments of the slip face.

Here we use the results of case no. 5 from *Omidyeganeh et al.* [2013], i.e., barchans spaced by 2.38λ (where λ is the length of the barchans along the wind direction and $\lambda = 3.62H$ where H is the crest height) on a grid $N_x \times N_y \times N_z = 384 \times 281 \times 512$. The large spacing of this case makes it similar to the case of an isolated

barchan. The model uses an immersed boundary method based on the volume-of-fluid technique [Hirt and Nicholas, 1981] to solve the Navier-Stokes equations at large (grid-resolved) scales. The significant mismatch in the Reynolds numbers between the LES simulation and natural flows over aeolian dunes has a twofold justification. First, turbulent flow after the separation of the flow and inside the mean recirculation bubble is dominated by the height of the dune and the reattachment length; hence, the scales of the flow structures in that zone are expected to be similar. Second, current LES models become exceptionally expensive, increasing as the number of grid points increases by $Re^{3/4}$ [Choi and Moin, 2012]. As such, some mismatch between modeled and natural Reynolds numbers is inevitable for large-scale flows given the computational capabilities available at present.

The turbulent shear stresses predicted by *Omidyeganeh et al.* [2013] were input to an infinite-slope-stability model to test the feasibility that turbulent shear stresses acting on the slip face can drive diurnal variations in the mean critical angle $\langle\theta_c\rangle$. It is the mean value of the critical angle that is most relevant here because both the driving and resisting stresses vary in space and time. The infinite-slope-stability model with a Mohr-Coulomb failure criterion predicts grain-flow initiation when the sum of turbulent and gravitational shear stresses exceeds the resisting stress, i.e.,

$$\tau_b + \rho_b gh \sin(\theta_c) > \rho_b gh \cos(\theta_c) \tan \phi \quad (6)$$

where ρ_b is the sand bulk density, g is the acceleration due to gravity, h is the depth of failure, and ϕ is the angle of internal friction. The first term on the left side of equation (6) represents the shear stress induced by turbulence, which can act both up and down the slope as indicated by the sign (negative values indicate stresses acting up the slope or against gravity). The second term on the left side is the static shear stress induced by gravity on the potential slide mass. The first term on the right side is the shear strength. When the turbulent shear stress acts down the slope, the slope can fail at lower slopes than would be possible with gravitational shear stresses alone. Earthquake triggering of landslides is a useful analogy for this hypothesized mechanism. During earthquakes, the component of shaking parallel to the slope induces a dynamic shear stress that can, acting in concert with gravity, cause landslides to be initiated at lower angles than is possible with gravity shear stresses alone [e.g., Gipprich et al., 2008].

2.4. Mass Balance Modeling of the Frequency of Avalanching and Its Relationship to Sediment Flux Coming Into the Slip Face and Changes in the Critical Angle With Time

In this section we derive a predictive equation for the frequency of avalanching of the slip face based on mass balance principles. First we consider avalanching driven by steepening of the slip face as a result of grain-fall deposition. The accommodation space (A) (Figure 1) that must be filled after an avalanche has just occurred before a new avalanche can be triggered can be estimated as

$$A = \frac{1}{2} plw \quad (7)$$

where l is the length of the zone of grain-fall deposition (modeled as a right triangle with maximum thickness at the brinkline), w is the maximum thickness of grain-flow deposition ($w = l \tan(\langle\theta_c\rangle - \langle\theta_r\rangle)$), and p is the fraction of sediment that accumulates on the upper slope that is advected to the bottom slope in a grain flow. The $1/2$ factor in equation (7) comes from the assumed right-triangular geometry of the grain-fall deposit. The factor p , which can theoretically vary between 0 and 1, is included because not all of the sediment that accumulates on the upper portion of the slope during the steepening phase is transported to the lower portion of the slope. In other words, p accounts for the fact that the minimum angle of the upper slope may be significantly greater than the angle of repose that develops on the lower half of the slope. We estimate that only about half of the sediment that accumulates on the upper portion of the slope is transported down the slope because semipermanent storage of some of the grain-fall deposits is required for the upper portion of the slip face to prograde along with the lower portion of the slip face; thus, we take p to be $\approx 1/2$. Under conditions of constant $\langle\theta_c\rangle$, the accommodation space generated by a grain flow must be filled by sediment transported over the brinkline before another grain flow can occur. By mass balance, the frequency of avalanching under such constant- $\langle\theta_c\rangle$ conditions is given by the volumetric unit sediment flux coming over the brinkline, q_w , divided by the accommodation space, A . We refer to this avalanche-driving process as the “accommodation-space-filling” component.

Variations in $\langle\theta_c\rangle$ through time can trigger grain flows even in the absence of sediment flux coming over the brinkline because the critical slope angle can become lower than the actual slope angle (even if this angle is not changing) provided that the critical angle is decreasing through time. If the critical angle is decreasing at a rate $d\langle\theta_c\rangle/dt$, avalanching will occur at a rate equal to $-(d\langle\theta_c\rangle/dt)/(\langle\theta_c\rangle - \langle\theta_r\rangle)$. To see this, consider the case in which $d\langle\theta_c\rangle/dt$ is negative. For each unit of time, the angle of the upper slope will decrease (by avalanching) by an amount equal to $d\langle\theta_c\rangle/dt$. Each time an avalanche is triggered, the mean critical angle must be further reduced by an amount equal to $\langle\theta_c\rangle - \langle\theta_r\rangle$ before the slip face again reaches the critical slope necessary to trigger another avalanche (in the absence of sand flux coming over the brinkline). For example, if $d\langle\theta_c\rangle/dt$ equals -1 h^{-1} and $\langle\theta_c\rangle - \langle\theta_r\rangle = 0.5^\circ$, the slope will avalanche at a rate equal to $-(d\langle\theta_c\rangle/dt)/(\langle\theta_c\rangle - \langle\theta_r\rangle)$ or 2 h^{-1} . The rate of change of the critical angle drives avalanching in a manner similar to that of a rotating drum half filled with sand [e.g., Yang *et al.*, 2015]. We refer to this avalanche-driving process as “rotational” because it is related to the change with time, or rotation, of the critical angle. If $\langle\theta_c\rangle$ increases with time, the frequency of avalanching driven by accommodation space filling, i.e., q_v/A , slows by an amount equal to $-(d\langle\theta_c\rangle/dt)/(\langle\theta_c\rangle - \langle\theta_r\rangle)$. Combining the accommodation-space-filling and rotational components of avalanching gives the following predictive equation for the frequency of avalanching, expressed as the fraction of the slip face area that experiences an avalanche per unit time:

$$R_r = \max\left(\frac{2q_v}{\rho l^2 \tan(\langle\theta_c\rangle - \langle\theta_r\rangle)} - \frac{d\langle\theta_c\rangle/dt}{\langle\theta_c\rangle - \langle\theta_r\rangle}, 0\right) \quad (8)$$

The max function in equation (8) is included to prevent the frequency of avalanching from becoming negative if $d\langle\theta_c\rangle/dt$ is large and positive. We assumed that the value of l is proportional to L , an assumption we test with available data in section 4.2. Lower values of l/L yield larger values of R_r , all else being equal. We constrained the average ratio l/L by matching the range of R_r values predicted by equation (8) with the range of measured frequencies of avalanching measured by the DoDs.

3. Results

3.1. Wind Speed, Sand Flux, and Grain-Diameter Measurements

Figure 3 illustrates the strong diurnal cycle of wind speed at the study site. Figure 4a plots the unit mass flux of sediment coming over the brinkline, q_s , as a function of the average shear velocity measured at three points along the crest (Figures 2b and 2c). The open circles represent data from two days (4 and 5 November) in which moisture played a significant role in the dynamics of saltation and/or grain flow. On the morning of 4 November a brief (approximately 30 min) low-intensity rainfall event occurred. The moisture input to the dunes from this event had a modest effect on aeolian sediment transport rates (i.e., sand fluxes are only slightly lower for 4 and 5 November relative to 6–9 November). However, the moisture had a dramatic effect on grain-flow activity for the next 2 days (discussed in more detail in section 3.4). Figure 4b plots d_{50} and d_{90} values from the saltating sand captured in the traps, and d_{90} is the particle diameter at 90% of the cumulative particle-size distribution. On the large dune the median grain size is approximately 0.2 mm and is independent of shear velocity. On the small dune the sand is a bit coarser ($d_{50} = 0.3\text{--}0.4\text{ mm}$) and shows a slight increase with increasing shear velocity.

Plots of time series data for shear velocity and sediment flux over the brinkline (Figures 5a and 5b) indicate that the shear velocity varies over a broad range from about 0 to 1.1 m s^{-1} , comparable to the total range of shear velocities analyzed by Sherman and Farrell [2008] using velocity profile data compiled from the literature. The pronounced increases in u_* and q_s are clearly revealed from 10:00 to 12:00.

3.2. TLS Measurements

3.2.1. Maps of Surface Change

Figure 6 illustrates the map products produced from the TLS data that serve as input to the analysis. Although grain flows vary widely in their morphology, the scars that grain flows leave behind on the upper slope and the deposits they emplace on the lower slope are typically 20–60 mm thick on both the large and small dune (Figure 7), i.e., 10–30 times greater than the accuracy of the instrument, and a thickness equivalent to about 100–300 mean grain diameters. The depths of scour and thicknesses of deposits on the small dune are slightly larger, on average, than those on the large dune, but this difference is only significant at the tail of the distribution (Figure 7). The range of deposit thicknesses we measured is consistent with those documented in the literature.

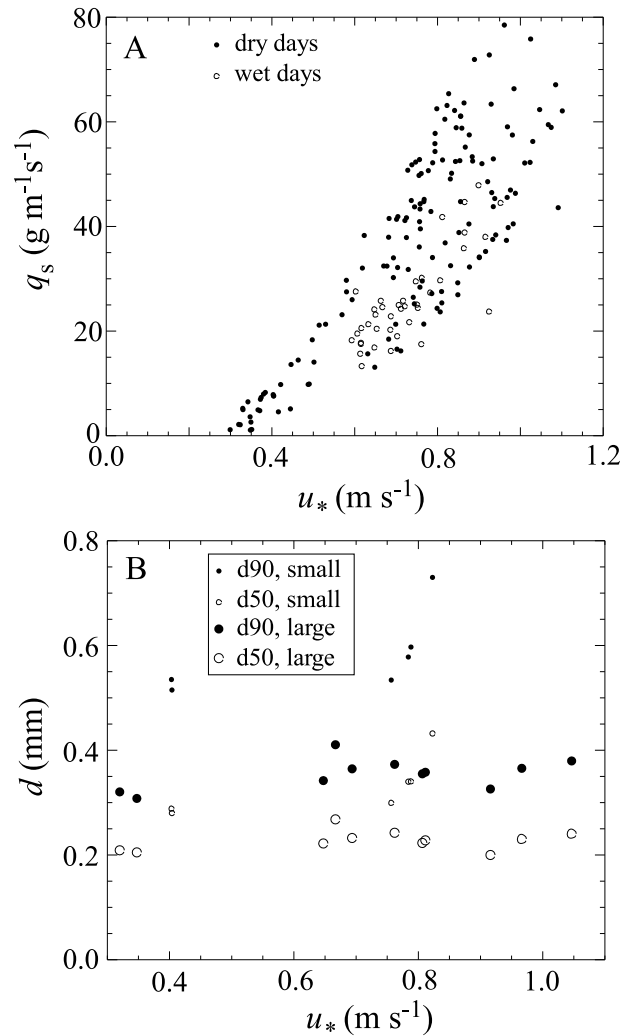


Figure 4. Measurements of flux and texture of sand in transport over the brinkline. (a) Mean unit sediment flux, q_s , over the brinkline as a function of shear velocity, u_* . Open circles indicate data from 4 and 5 November, the 2 days when significant soil moisture was present. (b) Plot of the median grain diameter, d_{50} , and the grain diameter of the 90th percentile, d_{90} , of sand in transport over the brinkline, as a function of shear velocity for the large and small dune experiment locations.

deposits (with some minor grain-flow reworking) accumulated on the top few meters of the slope. Figure 9b shows the morphology of an active grain flow (approximately 0.2 m wide, moving at $\sim 0.1 \text{ m s}^{-1}$) on the slope. Under fast wind conditions the majority of the grain flows traversed the entire length of the slope. Under the relatively slow winds of the early morning and late afternoon, many of the flows traversed only a portion of the total slope length.

DoD maps (Figure 10) demonstrate that grain-flow activity is more intense on the southern portion of the dunes than the northern portions as the wind speed increases each morning (Figure 10). Although Figure 10 shows just the first DoDs for each day, all of the DoDs collected between approximately 08:00 and 10:00 exhibited more grain-flow activity on the southern sides of the dunes. After approximately 10:00, no significant asymmetry was observed. This morning asymmetry is significant because it demonstrates that condensation and evaporation of morning dew (if present) are unlikely to be a significant driver of the diurnal cycle of grain-flow activity. Moisture increases the critical angle (see section 3.4). If morning condensation was affecting grain-flow activity, it would be expected to result in more, not less, grain-flow activity on the northern side of the slip face

Kocurek and Dott [1981], for example, reported maximum grain-flow thicknesses of 5–30 mm in ancient dune deposits of the Little Sahara dune field across a range of slip-face heights from 0.2 to 10 m. Grain-flow thicknesses in ancient aeolian sediments are compacted; hence, their thicknesses can be expected to be somewhat less than those of active dunes.

Figure 8 illustrates the diurnal cycle of slip-face evolution using a subset of the DoDs from 8 November as examples. Grain-flow activity increased steadily and rapidly from approximately 10:00 to 12:00 (Figures 8a–8c), then decreased (more slowly than the morning’s rate of increase) in the afternoon (12:00–16:00). After approximately 14:00, significant and persistent deposition on the upper slope occurs. Grain-flow activity (and hence erosion near the top of the slope) became negligible after approximately 16:00, even though sand transport persisted for some time thereafter, albeit at rapidly decreasing rates. Overnight and into the next morning, the slip-face evolution was entirely dominated by grain-fall deposition at the top few meters of the slope. The thickness of these deposits was up to 100 mm. Figure 8 shows the activity from just 1 day, but the temporal variations in grain-flow activity on the other dry days (6, 7, and 9 November) were quite similar.

Figure 9a shows the configuration of the slip face late in the day as wind speeds decreased and grain-fall

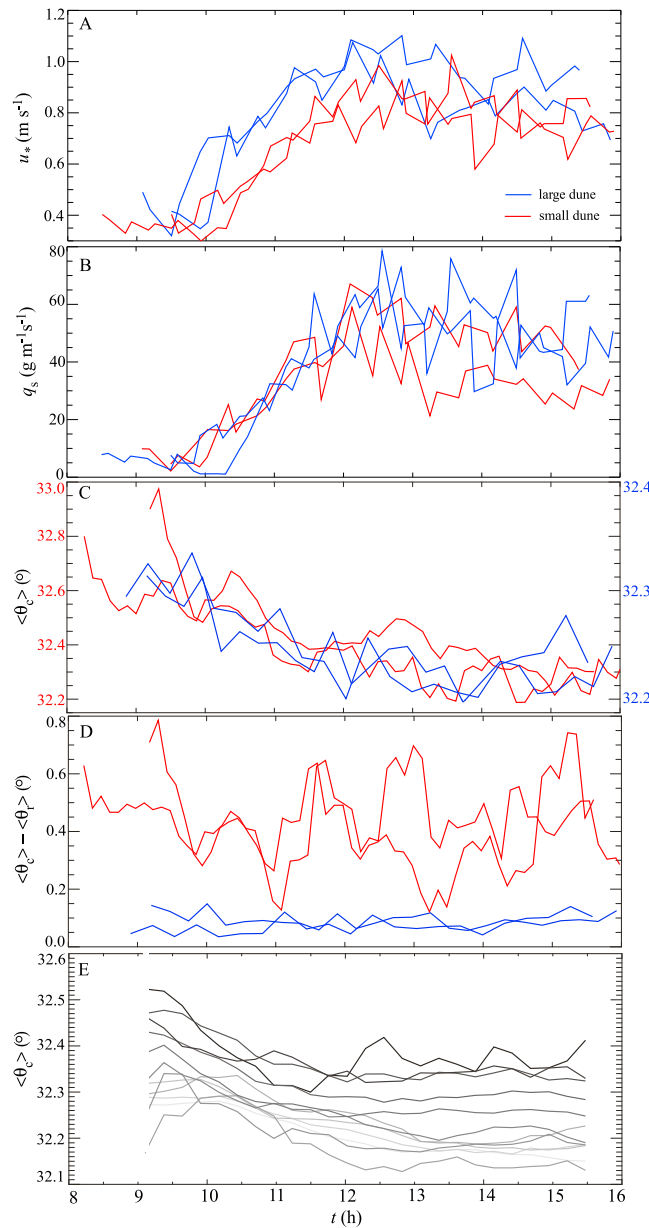


Figure 5. Plots of (a) shear velocity, (b) unit mass sediment flux, (c) mean critical angle, and (d) mean relaxation angle as a function of time for the four dry days (6–9 November). Blue and red line segments illustrate data from the large and small dunes, respectively. Note that in Figure 5c the y axis range of values differs between the large and small dune. (e) Plots of the mean critical angle measured in 1 m wide elevation bins versus time on 8 November for the top 12 m of the large dune. Darker gray lines represent higher elevations on the slip face.

DEMs of the slip face to obtain slope maps that were then analyzed to quantify the mean critical angle (using slopes values from areas that underwent erosion in the subsequent time interval) and the angle of repose (using slope values from areas that underwent deposition in previous time interval) and their variations through time. Instrument error limits the accuracy of elevation measurements and hence slope values. However, averaging the slope values computed at the DEM resolution (0.01 m and 0.02 m for the small and large dunes, respectively) over larger areas can result in precise estimates of mean slope values.

because much of the southern side is still in shadow before 10:00 while the north side is mostly in Sun. Therefore, any moisture that might condense on the slip face in the early morning would likely persist on the south side, thereby inhibiting grain-flow activity on that side. Our preferred explanation for the N-S asymmetry in grain-flow activity is that ESE winds, oblique to the barchan orientation, are dominant in the 08:00–10:00 time interval. This generates stronger flow recirculation—hence greater dynamic turbulent stresses—on the southern side of the dune relative to the northern side. Sand transport is also asymmetric. There is greater sand flux per unit length of the brinkline on the southern side because the orientation of the wind, and the resulting direction of sand transport, is closest to perpendicular to the slip face. Wind and sand transport become more oblique to the slip face as one moves northward along the brinkline, thus reducing sand flux per unit length of the brinkline in a manner analogous to that described by *Bauer and Davidson-Arnott* [2003]. Over much of the northern brinkline (and ignoring possible topographic steering) the ESE winds are blowing away from the slip face with the potential to transport sand toward what is ordinarily the stoss slope. When the wind shifts to the ENE direction and aligns with the orientation of the dune, the turbulent stresses on the north and south sides of the dune become similar and the sand flux becomes approximately symmetrical.

3.2.2. Variations in the Mean Critical Angle, Mean Angle of Repose, and the Frequency of Avalanching

In our analysis we differentiated

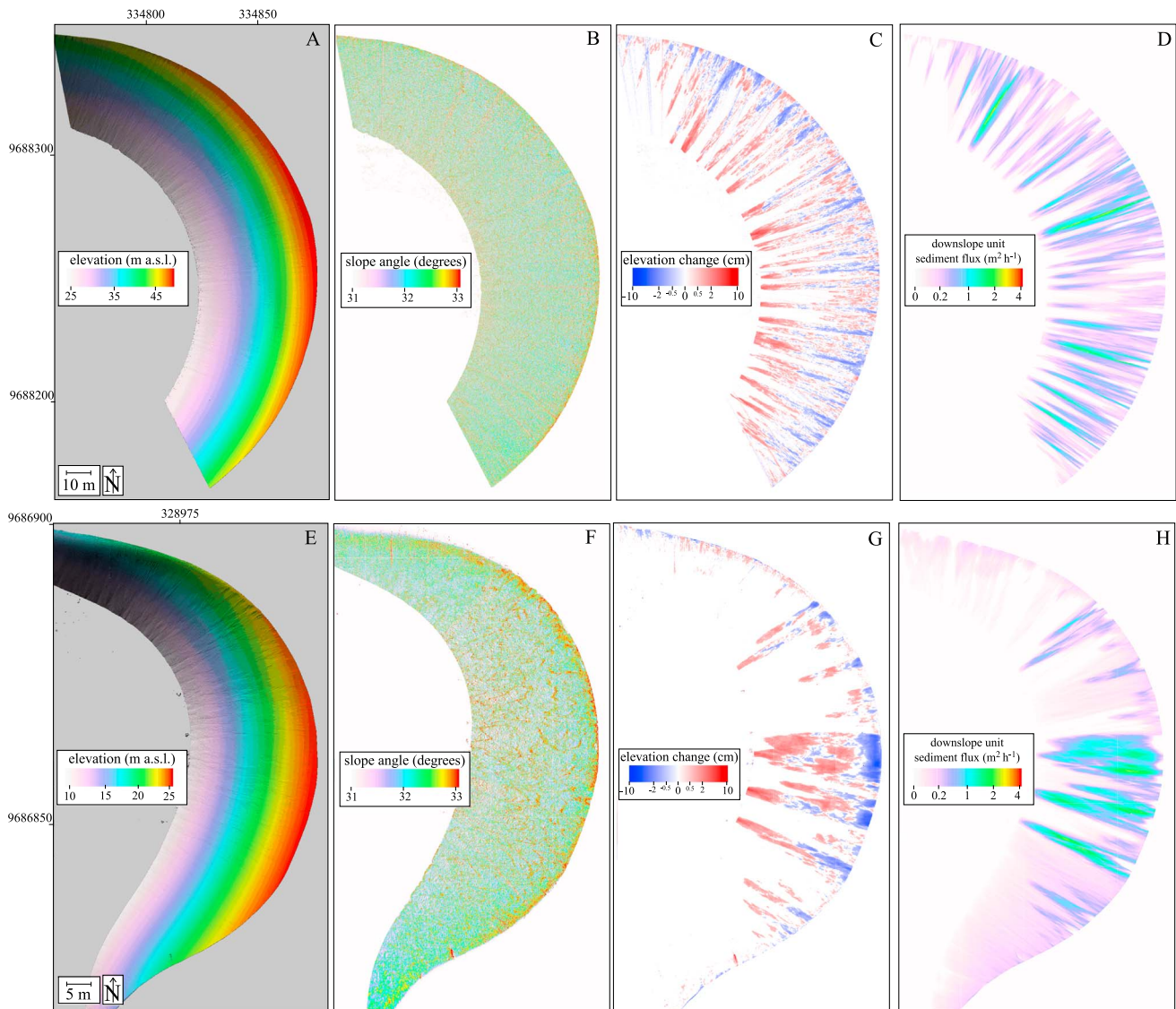


Figure 6. Color maps illustrating the types of data derived from terrestrial laser scanning (TLS). (a–d) Data for the large dune; (e–h) data for the small dune. Shaded-relief and color maps of slip-face elevations (Figures 6a and 6e), slope angles (Figures 6b and 6f), elevation changes over a 15 min interval (Figures 6c and 6g), and unit sediment fluxes (Figures 6d–6h) corresponding to the same intervals as Figures 6c and 6g.

Figures 11a and 11b illustrate the frequency distributions of the critical angle and angle of repose for a typical scan interval on the large and small dunes, respectively, during times of relatively fast winds. Slope values follow a Gaussian distribution. In samples that follow a Gaussian distribution, the uncertainty of the mean is given by the standard deviation divided by the square root of N where N is the number of samples used in the averaging. The standard deviation of the slope values computed at grid resolution is approximately 1.7° for both the large and small dune. The values of N vary somewhat from scan interval to scan interval but are $\sim 10^6$ for the large dune and $\sim 10^4$ – 10^5 for the small dune (e.g., $N = 1,853,078$ and $1,205,066$ for the data in Figure 11a and $N = 38,791$ and $88,996$ for the data in Figure 11b). As such, uncertainties in the mean values of the critical and repose angles are $\approx 2^\circ$ divided by ~ 1000 , or $\sim 0.002^\circ$, for the large dune, and $\approx 2^\circ$ divided by 100, or $\sim 0.02^\circ$, for the small dune. These values are representative of the accuracy of the mean slope values for all times because values of N are consistently $\sim 10^6$ for the large dune and $\sim 10^4$ – 10^5 for the small dune.

The data illustrated in Figure 11 demonstrate a key conclusion of this study, i.e., that the mean critical angle is slightly but significantly lower on the large dune relative to the small dune. A two-tailed t test for unpaired

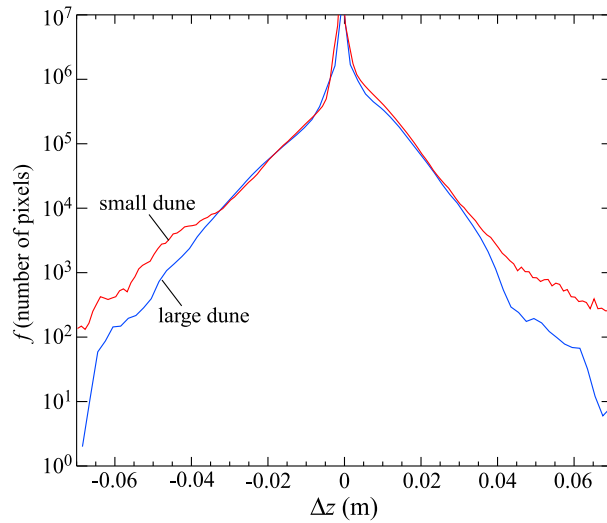


Figure 7. Plots of the frequency of occurrence of elevation changes, Δz , from the large (blue curve) and small (red curve) dunes. These data show that the vast majority of grain flows involve local elevation changes in the 20–60 mm range. Grain flows are slightly thicker, on average, on the smaller dune. Note that magnitudes of change below approximately 5 mm are not significant (i.e., they are indistinguishable from zero).

with computing the slope values by differentiating coarser grids in order to lower the uncertainty of the mean values of the critical and repose angles. This decreases the standard deviation of the data in plots such as Figure 11 because the standard deviation is approximately equal to the mean instrumental error of the elevation measurements (i.e., ≈ 1 mm) divided by the horizontal distance over which the slope is computed, which we chose to be 0.02 m for the large dune and 0.01 m for the small dune but which could have chosen to be larger. Choosing a larger horizontal distance does not improve (i.e., lower) the uncertainty of the mean values of the critical and repose angles, however, because any reduction in the standard deviation of individual slope measurements is negated by the reduction in the number of samples available for averaging.

Figures 5c and 5d plot time series data for the mean critical angle and relaxation angle for the four dry days (6–9 November). A total of 203 estimates of the mean critical angle and angle of repose was obtained from the TLS data (one for each scan interval). These data demonstrate that the value of $\langle \theta_c \rangle$ decreases steadily during each day (rapidly at first, then more slowly) before increasing slightly at approximately 16:00. Under fast wind conditions the value of $\langle \theta_c \rangle$ was $\approx 32.2^\circ$ for both the large and small dune. Under slow wind conditions the large dune had $\langle \theta_c \rangle \approx 32.35^\circ$, while the small dune had $\langle \theta_c \rangle \approx 33^\circ$. The values of the relaxation angle $\langle \theta_c \rangle - \langle \theta_r \rangle$ did not vary systematically with time on either dune. The values of $\langle \theta_c \rangle - \langle \theta_r \rangle$ were smaller for the large dune, i.e., the large dune had $\langle \theta_c \rangle - \langle \theta_r \rangle$ values ranging from 0.05° to 0.15° , while the smaller dune had $\langle \theta_c \rangle - \langle \theta_r \rangle$ values ranging from 0.2° to 0.8° .

We also computed the means of the critical angle and angle of repose by averaging local values in 1 m elevation bins to test whether the decrease in the value of $\langle \theta_c \rangle$ with increasing shear velocity occurs robustly up and down the slip face. They do. As an example, Figure 5e plots $\langle \theta_c \rangle$ values computed for 1 m elevation bins on the upper half of the large dune versus time and elevation for 8 November. These plots demonstrate that the decrease in $\langle \theta_c \rangle$ with time occurs everywhere on the top half of the dune. We did not analyze the bottom half of the slip faces for spatiotemporal variations in $\langle \theta_c \rangle$ because these areas are dominated by deposition and hence lack a sufficient number of points to enable precise estimates of $\langle \theta_c \rangle$.

Figure 12a plots the frequency of avalanching as a function of time for 6–9 November. If the frequency of avalanching were only controlled by the accommodation-space-filling component of equation (8), the frequency of avalanching would be negligible before approximately 10:00 each morning (because sand flux is minimal before this time (Figure 5b)) and it would reach a maximum approximately 12:00–14:00 every day when the

data indicates that the critical angles for the large and small dunes are not drawn from the same population ($t = 35.2$, $P < 0.0001$), whereas the angles of repose are likely to have been ($t = 1.15$, $P = 0.25$). Because uncertainties in the mean critical angles are consistently $\sim 0.002^\circ$ for the large dune and $\sim 0.02^\circ$ for the small dune, differences in mean critical or repose angles as a function of time that are many times larger than 0.002° (for the large dune) or 0.02° (for the small dune) are statistically significant.

We wish to emphasize that the variance in the data plotted in Figure 11 is primarily a function of the distance over which the slope is computed, i.e., 0.02 m for the large dune and 0.01 m for the small dune, and not primarily a property of the physical system. We experimented

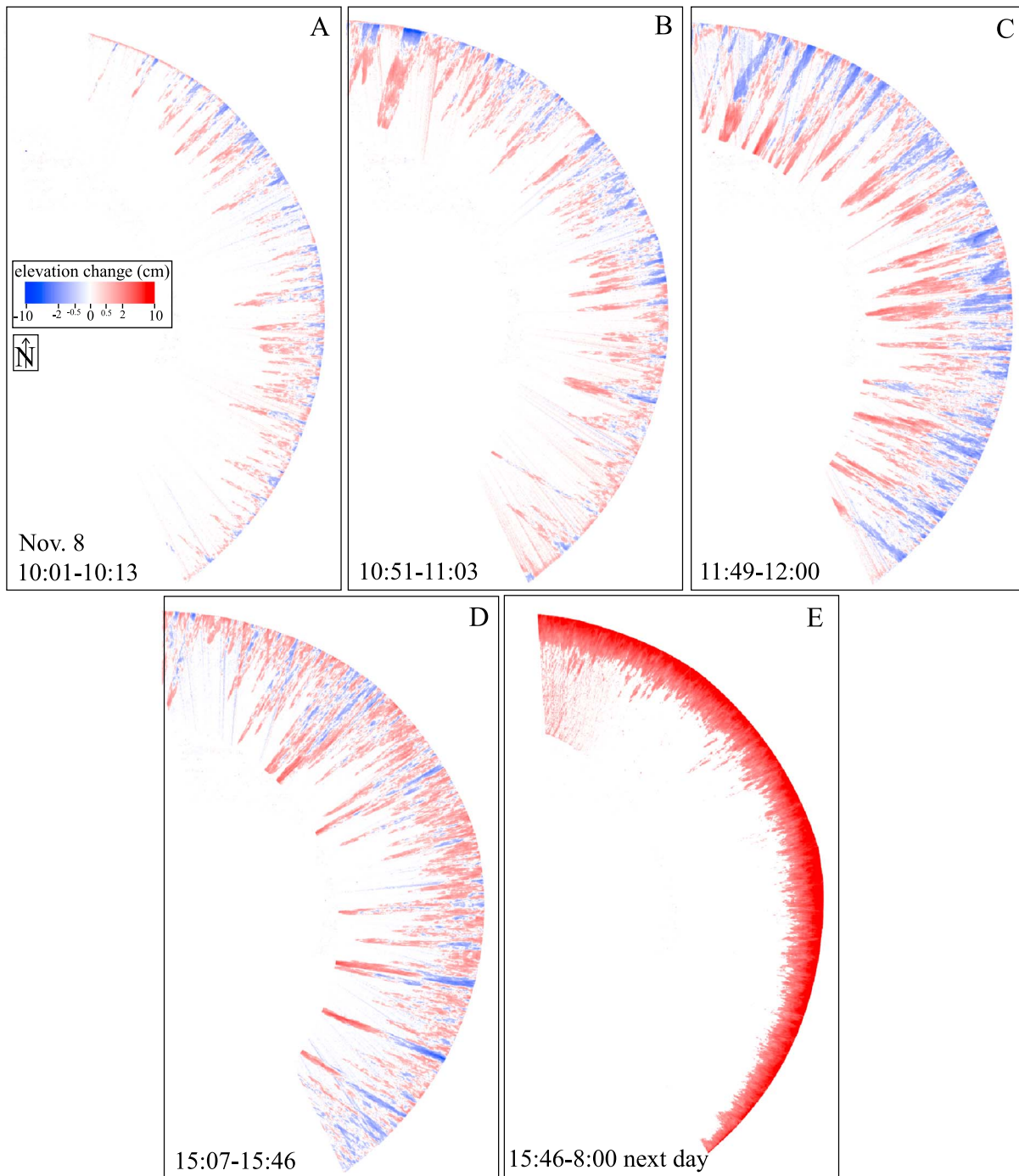


Figure 8. Color maps of elevation changes for select intervals of a dry day on the large dune (8 November).

sand flux reaches a maximum. Instead, the frequency of avalanching is substantial ($1\text{--}2\text{ h}^{-1}$) well before 10:00 each morning and the maximum frequency of avalanching occurs before noon on two of the 4 days. On the large dune there was 1 day (6 Nov) when the maximum frequency of avalanching ($\approx 2.3\text{ h}^{-1}$) occurred approximately 10:30 and another day (8 November) when the maximum in the morning (approximately 10:30) was comparable to the maximum in the afternoon (approximately 13:00). On the small dune the maximum avalanche rate occurred in the morning (11:30) on 7 November and in the early afternoon (12:00–13:00) on 9 November.

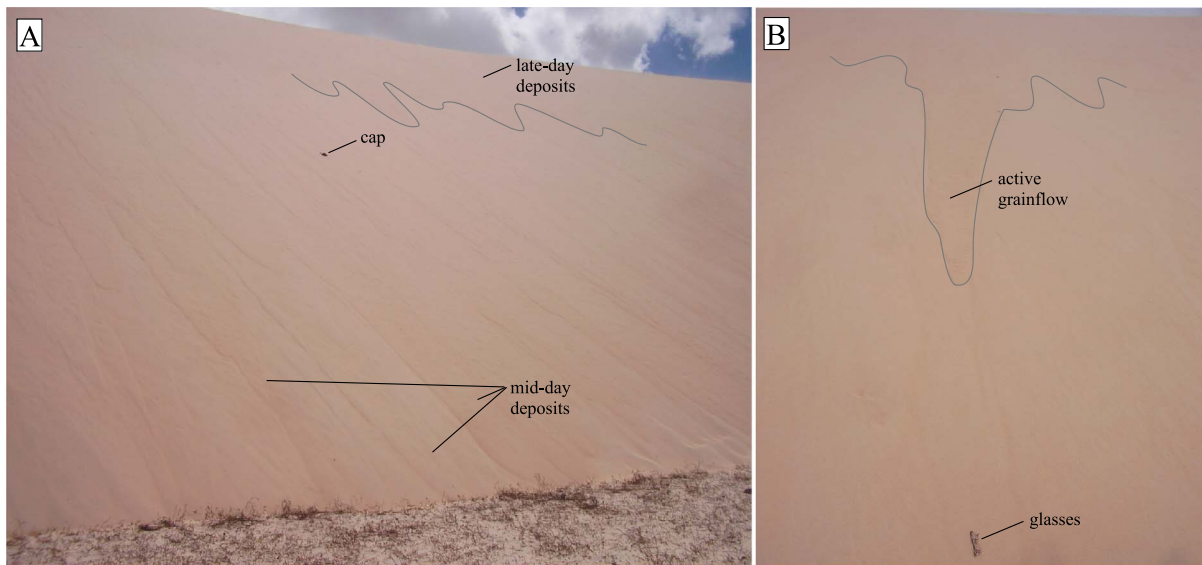


Figure 9. Field photographs illustrating (a) the multiple generations of deposits and (b) the morphology of an active grainflow.

Decreases in $\langle \theta_c \rangle$ and the frequency of avalanching with time each morning closely track the increase in shear velocity. A key hypothesis of this paper is that higher shear velocities lead to an increase in the magnitude of turbulent shear stresses that act randomly up and down the slip face, at times acting in concert with gravitational stresses to trigger grain flows at lower slope angles than would otherwise be possible. To test this hypothesis, together with the predictions of the mass balance model for avalanching formalized as equation (8), we used equation (8) to quantify the theoretical frequency of avalanching using TLS-derived data for $\langle \theta_c \rangle$ and $\langle \theta_c \rangle - \langle \theta_r \rangle$ as input to equation (8) assuming $P=0.5$. We also used time series data for q_s (after converting to q_v using the bulk density 1500 kg m^{-3}) and $\langle \theta_c \rangle - \langle \theta_r \rangle$ (plotted in Figures 5b and 5d) as inputs to equation (8). In order to quantify $d\langle \theta_c \rangle/dt$ for input to equation (8), we represented the temporal

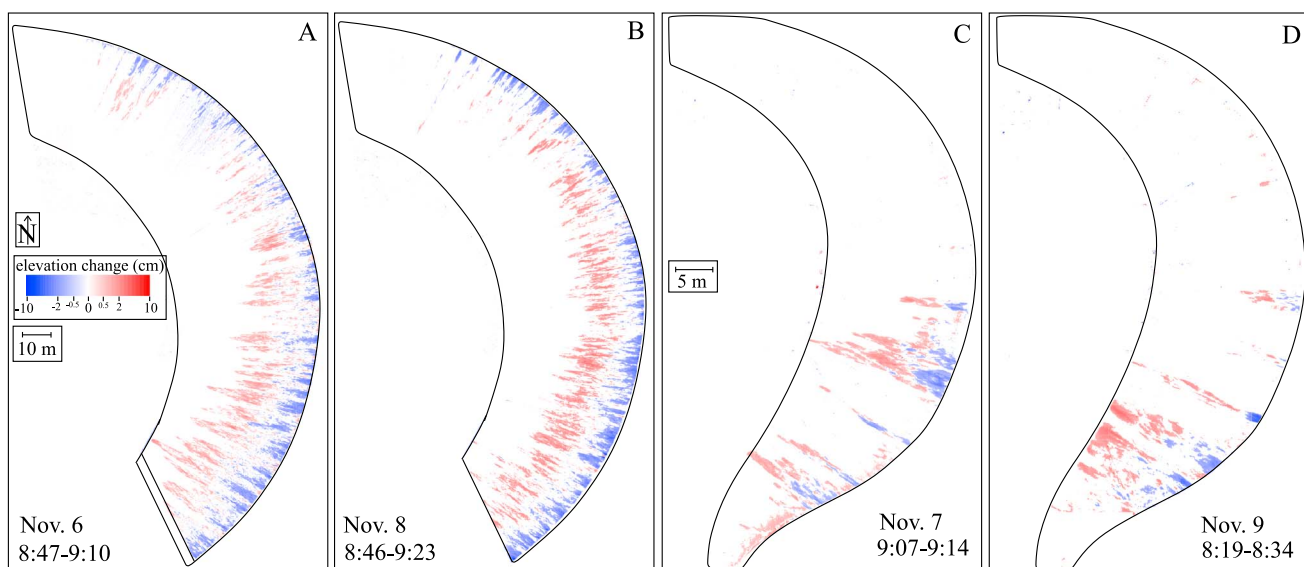


Figure 10. Color maps of topographic change for the first survey of the morning on each of the four dry days, illustrating the predominance of grain-flow activity on the southern portion of the dunes in the morning in the approximately 08:00–10:00 time interval. (a and b) large dune; (c and d) small dune. The approximate slip-face outline is shown in black.

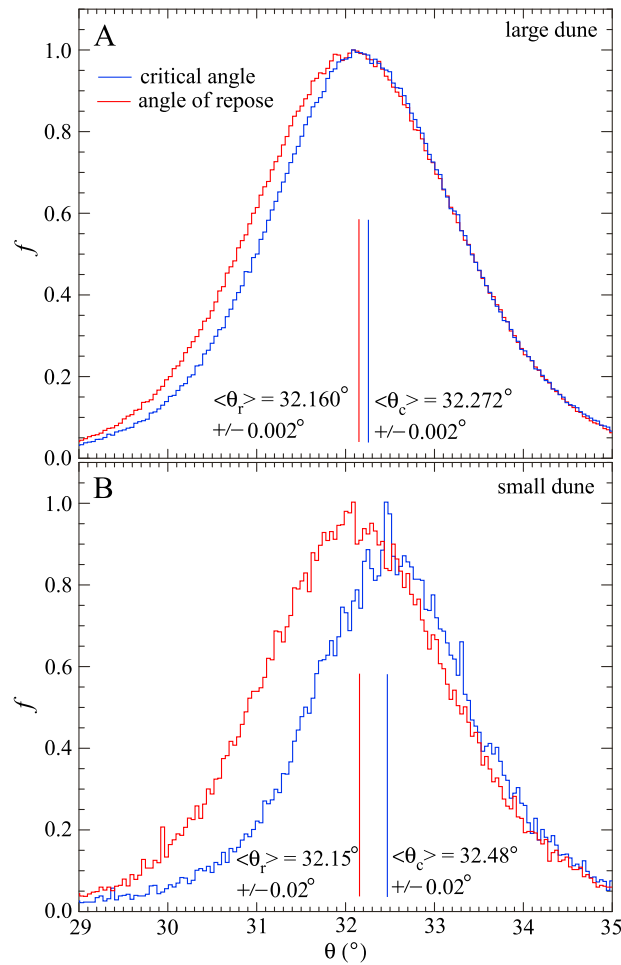


Figure 11. Example distributions (i.e., plots of relative frequency) of the critical angle (in blue) and the angle of repose (in red) measured for the (a) large and (b) small dunes. Also shown are the mean values (with uncertainties) for each distribution.

variations in $\langle \theta_c \rangle$ using a sinusoidal function (i.e., the same function that appears as a dashed curve in the wind-speed plot of Figure 3):

$$\langle \theta_c \rangle = \langle \theta_{c,\min} \rangle + (\langle \theta_{c,\max} \rangle - \langle \theta_{c,\min} \rangle) \left(\cos\left(\frac{2\pi(t-3)}{24}\right) + 1 \right) \quad \text{for } 8 \leq t \leq 16 \quad (9)$$

where t is time in the hour of the day (0 is midnight) and $\langle \theta_{c,\max} \rangle - \langle \theta_{c,\min} \rangle$ was estimated to be 0.15° for the large dune and 0.8° for the small dune based on the maximum range of measured variations (Figure 5c). We adopted this approach rather than differentiating the data in Figure 5c directly because the short-term fluctuations in $\langle \theta_c \rangle$ values would result in large positive and negative excursions in $d\langle \theta_c \rangle/dt$. By using equation (9), we are quantifying $d\langle \theta_c \rangle/dt$ at time scales relevant for avalanching, i.e., greater than or equal to several hours.

The frequency of avalanching predicted by equation (8) (Figure 12b) closely matches the measurements in Figure 12a in terms of the broad pattern of change during the day, i.e., relatively low frequency of avalanching early (approximately 08:00–09:00) and late (approximately 15:00–16:00) each day with higher rates in the late morning and/or early afternoon. The similarity between the absolute rates is not significant because we varied the ratio l/L to match the range of predicted frequencies of avalanching with the measured range, i.e., $0.5\text{--}3\text{ h}^{-1}$ (Figure 12a). The best match occurred with $l/L = 0.37$, indicating that, on average, the length scale of grain-fall deposition is slightly more than one third of the total length of the slip face. Figure 12c plots the ratio of the rotational component of avalanching (i.e., the component due to changing $\langle \theta_c \rangle$ values through time) to the total frequency of avalanching from both rotational and accommodation-space-filling components. This plot

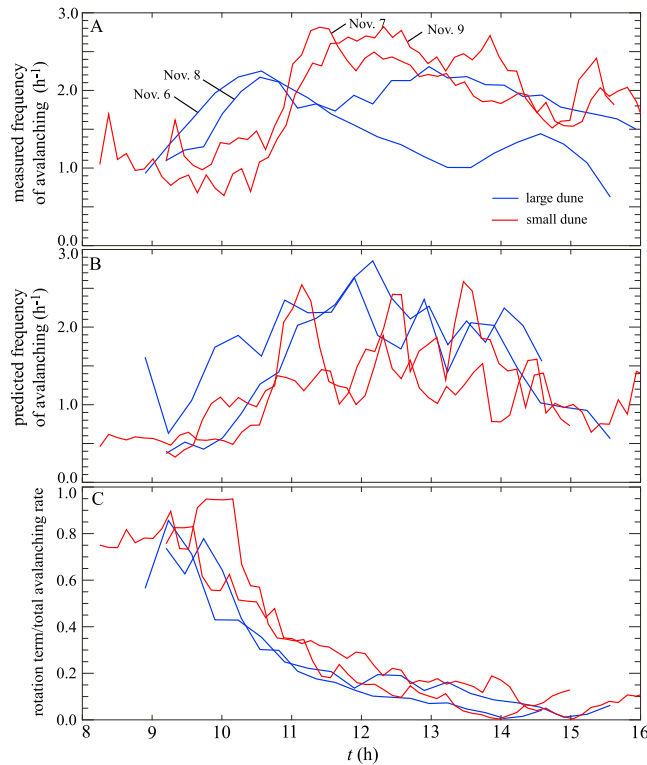


Figure 12. Plots of (a) measured frequency of avalanching, (b) predicted frequency of avalanching (from equation (8)), and (c) the ratio of the rotational component of the frequency of avalanching to the sum of the rotational and accommodation-space-filling components.

figure clearly illustrates the storage of sediment on the top portion of the slope during some times (e.g., approximately 10:00, 12:00, 13:30, and 15:00), followed by advection of a portion of those sediments down the slip face. An increase in the frequency of avalanching from the late morning to the afternoon is also apparent.

3.3. Computational Fluid Dynamics Modeling and Infinite Slope Stability Analysis

Figure 14a plots the magnitude of the mean, $\bar{\tau}_b$, and standard deviation, σ_{τ_b} , of turbulent bed shear stresses predicted by the 3-D large eddy simulation (LES) model of *Omidyeganeh et al.* [2013] as a function of horizontal distance from the brinkline along the dune centerline, x . The results are presented normalized by the far-field velocity, U_∞ . The far-field velocity corresponding to relatively fast winds is approximately 30 m s^{-1} based on the typical range of shear velocities measured over macroscopically flat surfaces in Jericoacoara (i.e., $u_* = 0\text{--}1 \text{ m s}^{-1}$) and z_0 values of $\sim 1 \text{ mm}$, assuming that the far-field height is 10 times the height of the dune or $\sim 300 \text{ m}$. Figure 14b plots the frequency distribution of bed shear stresses acting on the slip face assuming the Gaussian or near-Gaussian distribution of velocity fluctuations typically found in fully developed turbulence [e.g., *Chu et al.*, 1996], for four positions along the slip face and for two values of U_∞ associated with relatively fast wind conditions.

Figure 14b demonstrates that all portions of the slip face (which extends from $x/H = 0$ to 1.84, where H is the slip-face height) experience shear stresses in the downslope direction (i.e., acting with gravity) in the range of 0–5 Pa under relatively fast wind conditions. Larger shear stress values occur less frequently, but even a 0.1% fraction of occurrence is significant when grain flows occur $\sim 1 \text{ h}^{-1}$ and only require $\sim 1 \text{ s}$ of high shear stress to trigger failure. The largest shear stresses in the downslope direction occur on the upper slope where bed shear stresses up to 8 Pa can occur with a frequency equal to 0.1% of the time. It is during these events when the slip face can fail at lower slope angles than it otherwise would.

demonstrates that the rotational component is dominant in driving avalanching before approximately 10:00 when the sediment flux coming over the brinkline is relatively low and the winds are gaining speed (thus rapidly lowering $\langle \theta_c \rangle$). Conversely, in the late morning and afternoon the accommodation-space-filling component of equation (8) becomes dominant as $\langle \theta_c \rangle$ stabilizes at the relatively low values characteristic of fast winds and the high sediment fluxes repeatedly and rapidly fill the accommodation space on the upper slope, triggering avalanches.

The storage-and-release process on the slip face can also be quantified and visualized by plotting the mean sediment flux down the slope as a function of height above the base of the slip face and time. The average flux within 1 m elevation bins was computed and then plotted as function of height above the base of the slip face and time. Figure 13 shows where on the slip face of the large dune sediment flux is occurring as the day progresses. This

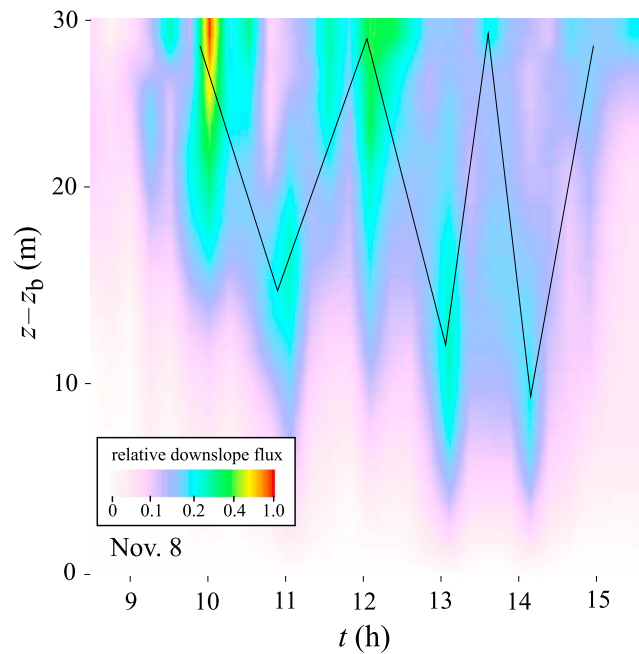


Figure 13. Color map constructed from all of the flux maps obtained on 8 November (example in Figure 6d), illustrating the average unit sediment flux by grain flows as a function of the height above the base of the slip face, $z - z_b$ (where z_b is the elevation of the base) and time during the day. This map illustrates the cyclic nature of the storage-and-release process, with periods of steepening/storage on the top portion of the slope followed by advective transport of a portion of those deposits down the slope. The black lines are included simply to highlight the oscillating nature of the flux as the slope shifts from storage to release phases.

dramatically different from the four dry days. Analysis of the bulk sand samples indicated that there was 1% moisture content in the sand, but the effect on transport rates was substantial. For similar shear velocities, the sand transport over the brinkline on the wet days was reduced to about 70% of that measured during dry conditions. Figures 15a and 15b show DoDs corresponding to the total change between approximately 08:00 and 16:00 on 4 and 5 November. Grain flows occurred on 4 November (the deposition visualized in Figure 15a is mainly though not strictly grain-fall deposition), but the increase in effective viscosity of the sand associated with moisture resulted in very limited transport distances once a grain-flow was initiated. Indeed, no grain flows made their way to the bottom half of the slip face. Fewer grain flows were initiated (and they were initiated on only a fraction of the total area of the slope) because the moisture increased the granular cohesion because of surface tension, and resulted in a large increase in $\langle \theta_c \rangle$ (Figure 15c). In turn, this increased the cross-sectional area of the accommodation space that had to be filled before grain flows were triggered. A small but detectable decrease in elevation occurred on the lower half of the slip face (i.e., lower than where any grain-flow deposition occurred) on this day, most likely as a result of wetting-induced compaction of the static dune sands during the rain event. This decrease also contributed to enlargement of the accommodation space. The value of $\langle \theta_c \rangle$ for 4 November exceeded 33.5° on the upper portion of the slope (Figure 15c), an average much larger than the maximum 32.35° on the dry days of 6 and 8 November. As a result of the increase in accommodation space, the frequency of avalanching on 4 and 5 November was less than 0.5 day^{-1} or 1–2 orders of magnitude lower than the frequency of avalanchings measured on 6–9 November. At the end of the day on 5 November some of the lowest portions of the slip face had not experienced any deposition for two full days (Figure 15b). The effects of moisture were still significant on 5 November but less dramatic than on 4 November, consistent with the idea that drying of the sands reduced the effects of moisture on the slip-face change. On 5 November the $\langle \theta_c \rangle$ value was reduced from 33.5° to the range of 32.5° – 33.0° (Figure 15c) and most of the sediment stored on the upper portion of the slope on 4 November was advected down to near the bottom of the slope.

The approximate magnitude of turbulent shear stress values can be input to the infinite-slope-stability model to test the feasibility that variations in $\langle \theta_c \rangle$ are driven by diurnal cycles of turbulent shear stress magnitudes. An increase in the value of $\langle \theta_c \rangle$ equal to 0.3° (i.e., the maximum diurnal range of $\langle \theta_c \rangle$ in Figure 5c) is equivalent to an increase in the normal stress of 5 Pa for a flow initiated 60 mm below the surface (i.e., a typical maximum depth of failure on both the large and small dune according to Figure 7). This value for the dynamic shear stress is consistent with the values predicted by the computational fluid dynamics modeling. Thus, the temporal variations in turbulent shear stresses have the capacity to drive variations in $\langle \theta_c \rangle$, which, in turn, drive a significant portion of the grain-flow activity during the morning at our study sites.

3.4. Sand Moisture Control of Internal Friction

The slip-face evolution on the two “wet” days (4 and 5 November) was

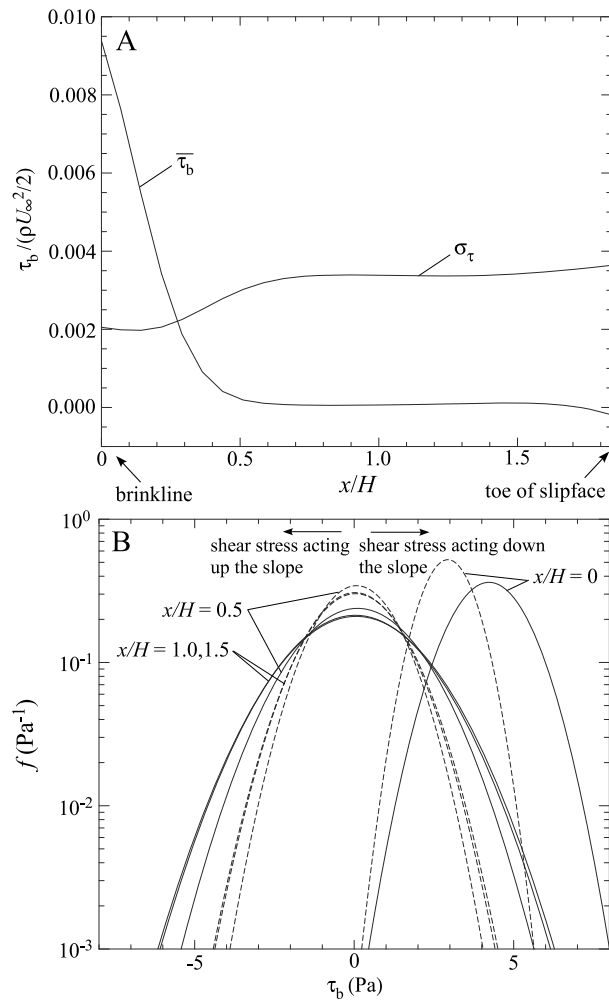


Figure 14. Bed shear stress acting on the slip face as predicted by the 3-D large eddy simulation (LES) model of *Omidyeganeh et al.* [2013]. (a) Plot of the mean, $\bar{\tau}_b$, and standard deviation, σ_τ , of turbulent bed shear stresses, normalized by the density of air, ρ , and the square of the far-field velocity, U_∞ , as a function of horizontal distance from the brinkline along the dune centerline, x . (b) Frequency of bed shear stress predicted by the model for four slip-face locations ($x/H = 0, 0.5, 1.0, 1.5$) and two values of the far-field velocity ($U_\infty = 25 \text{ m s}^{-1}$ (dashed curve) and 30 m s^{-1} (solid curve)). Positive values act down the slope, i.e., with gravity, while negative values act up the slope.

4. Discussion

4.1. Evidence for the Role of Turbulent Shear Stress in Modulating the Mean Critical Angle

Multiple lines of evidence support the hypothesis that there is a diurnal cycle of changes in the mean critical angle, $\langle \theta_c \rangle$, and that this cycle is driven primarily by diurnal variations in wind speed that increase the turbulent shear stresses acting on the slip face during late mornings and afternoons. First, the data show a clear inverse relationship between $\langle \theta_c \rangle$ and shear velocity (Figure 5). Second, 3-D LES modeling predicts magnitudes of turbulent shear stresses acting on the slip face with a range of values consistent with those needed to explain the measured diurnal variations in $\langle \theta_c \rangle$ via the infinite slope-stability criterion of equation (6) (Figure 14). Third, the N-S asymmetry in grain-flow activity observed in the morning coincides with the shift in wind direction from ESE (oblique to the dune centerline) to ENE (along the dune centerline) (Figure 10). The relationships among the key variables defining slip-face evolution and their diurnal variation are summarized in Figure 16.

Critical angles for granular materials can vary significantly depending on grain size [Brown and Richards, 1966; Robinson and Friedman, 2002]. As such, an alternative hypothesis for changes in $\langle \theta_c \rangle$ is that faster shear velocities could modulate $\langle \theta_c \rangle$ via

changes in the sizes of grains transported over the brinkline. However, we observed no significant correlation between the sizes of grains coming over the brinkline and shear velocity (Figure 4b), so temporal variations in grain size are unlikely to be a significant factor in controlling the frequency of avalanching. We did find, however, that even relatively small moisture content in the dune sands can increase $\langle \theta_c \rangle$ substantially, i.e., 1% moisture content increased the critical angle by more than 1° compared to that of dry conditions.

The sensitivity of the critical angle to the magnitude of turbulent stresses might be one manifestation of the effect of the steep slope in reducing the threshold shear velocity necessary to entrain lee slope sand [e.g., Howard, 1977; Iversen and Rasmussen, 1999]. This implies that avalanching would be initiated by the motion of individual grains at the surface. Our observations of avalanches, however, indicate that the initial stages of movement are more akin to slab failure, with the locations of grains on the surface of the avalanche static relative to one another. This suggests that the initiation of grain flow is more likely related to the failure of internal force chains [e.g., Ostojic et al., 2006] than to the initiation of motion by wind.

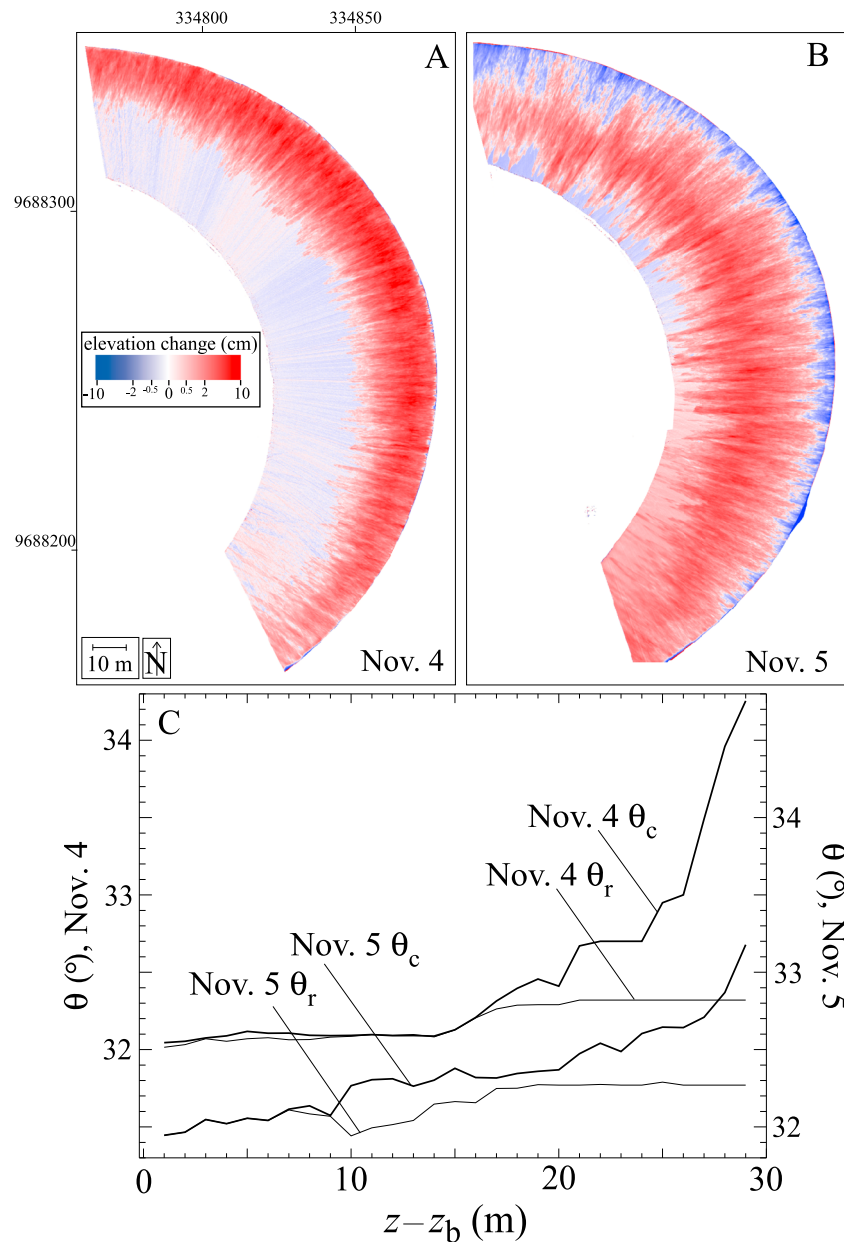


Figure 15. (a–c) Illustration of the effects of sand moisture on storage-and-release dynamics. A rainstorm on the morning of 4 November led to an approximately 1° increase in $\langle \theta_c \rangle$ (Figure 15c). The result of this increase is that no grain flows occurred on that day, only aggradation of the upper portion of the slope. After some drying of the sand occurred, the $\langle \theta_c \rangle$ value decreased, which triggered sediment redistribution from the upper portion of the slope to the middle and bottom portions by grain flows.

4.2. Controls on the Frequency of Avalanching

Our data are broadly consistent with the results of *Sutton et al.* [2013a, 2013b], who found that the frequency of grain flows generated in a laboratory dune depended on the sediment flux over the brinkline (formalized in our equation (8)). They also demonstrated that the relaxation angle controls the frequency of quasiperiodic cycles of storage and release of sediment from the upper slope in a manner that is also consistent with our equation (8). Our results, however, document that there is an additional term related to changes in the mean critical angle through time that controls the frequency of avalanching. Such rotational changes are the dominant control on the frequency of avalanching before approximately 10:00 in the morning at our study site (Figure 12c).

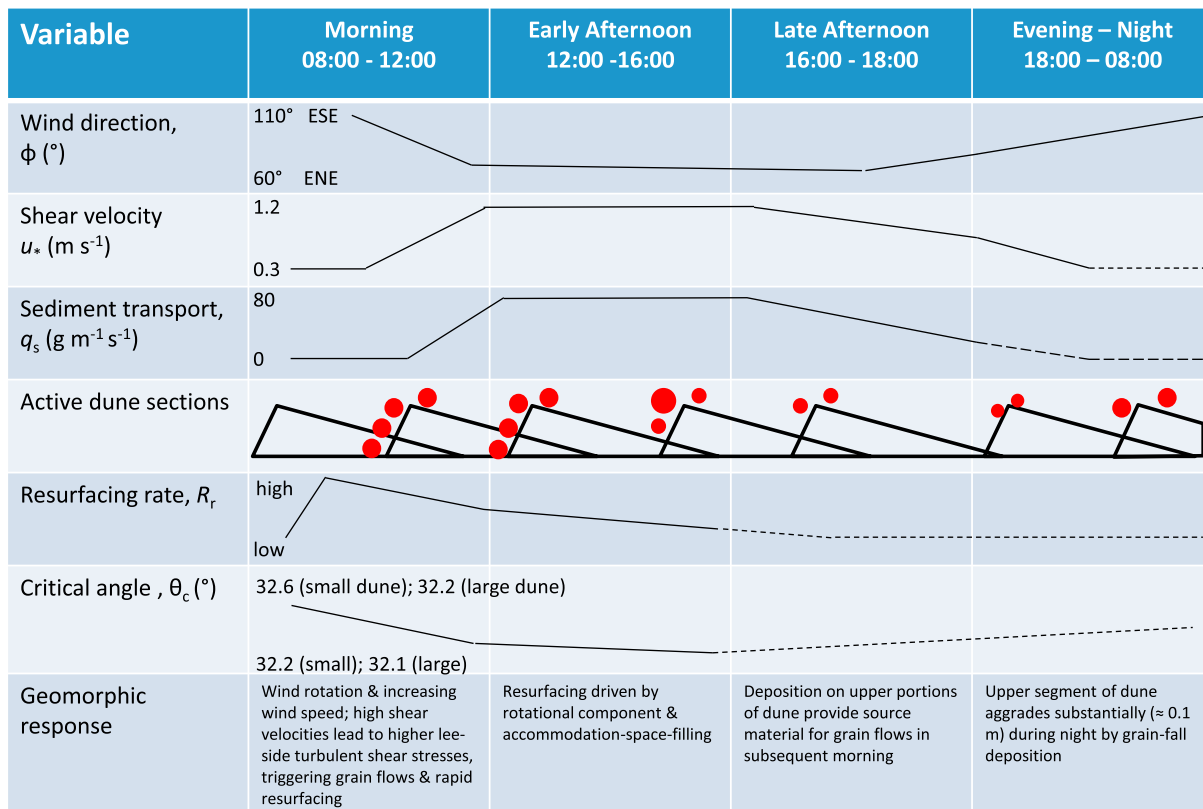


Figure 16. Summary of key variables of slip-face evolution and their diurnal variations at the study site under dry conditions.

The conceptual model of this paper (Figure 1) assumes that the length scale of grain-fall deposition, l , is proportional to the length of the slip face, L . It is clear, however, that the length scale of grain-fall deposition varies with wind speed such that there are times when grain-fall deposition is limited to the top few meters of the slip face, especially during slow winds (e.g., Figure 8e). Our DoD maps do not allow us to quantify the length scale of grain-fall deposition as a function of time or dune size because such changes are superimposed on the changes related to avalanching. Nonetheless, the available data suggest that grain-fall deposition occurs on most of the upper slip face during the fast winds that dominate transport at our study site. That grain-fall deposition can occur on a large fraction of the upper slip face during fast winds is shown by the DoD map in Figure 15a. This change map, recorded on 4 November when we observed minimal grain-flow activity due to the moist sand, shows that deposition occurred on the upper one third to one half of the large dune. DoD maps of both the large and small dunes (Figures 6 and 8) show that the upper one third to one half of both dunes is dominated by erosion (areas in blue) over time scales less than ~ 1 h (consistent with the l/L value of 0.37 we obtained by matching the range of predicted and measured frequencies of avalanching), except in the morning when the grain-fall deposits stored on the slope overnight begin to be mobilized. To the extent that erosion occurs predominantly in areas that have been superelevated by grain-fall deposition, these maps suggest that both the large and small dunes have a similar proportion of their slip faces affected by grain-fall deposition. One reason why the length scale of grain-fall deposition, l , may tend to be larger on larger dunes is that the speed-up ratio of a large dune is greater than that of a small dune under the same regional wind forcing [e.g., Bo and Zheng, 2013]; hence, grains can be expected to be launched over the brinkline with a higher velocity on a large dune relative to a small dune. Alternatively, the apparent dune-size dependence of the grain-fall length scale may reflect the nature of lee-side wake structures that should scale with dune height, as suggested by Walker and Nickling [2002]. Our results are also supported by the findings of Nickling et al. [2002], who found that the distance of downwind distribution of grain fall increased with wind speed and with dune height, patterns that they attribute to the role of turbulence in the dune wake.

Variations in the proportion of the slip face affected by grain-fall deposition are a complicating factor in this study but are unlikely to be a cause for any of the patterns we observed. Under relatively slow wind speeds, the proportion of the slip face affected by grain-fall decreases, accommodation space is hence reduced, therefore the frequency of avalanching would be expected to have an inverse dependence on wind speed, all else being equal. Our data show the opposite trend; i.e., the frequency of avalanching increases with wind speed. Figure 5e demonstrates that the decrease in the mean critical angle with increasing shear velocity occurs for all portions of the slip face, not just for one segment; hence, it is not caused by variations in the proportion of the slip face affected by grain-fall deposition. If the length scale of grain-fall deposition was responsible for the dependence of relaxation angle on slip-face height, one would expect to see some difference in the relaxation angle as a function of wind speed or time of day. Instead, aside from temporal fluctuations, the mean relaxation angle is larger on the small dune than the large dune at all times of the day.

4.3. Dependence of the Critical and Relaxation Angles on Slip-Face Height

The data presented in this paper demonstrate that $\langle\theta_c\rangle$ and $\langle\theta_c\rangle - \langle\theta_r\rangle$ depend on the slip-face height. The larger dune had $\langle\theta_c\rangle$ values ranging from 32.2° to 32.35° and $\langle\theta_c\rangle - \langle\theta_r\rangle$ values ranging from 0.05° to 0.15°, while the smaller dune had $\langle\theta_c\rangle$ values ranging from 32.2° to 33° and $\langle\theta_c\rangle - \langle\theta_r\rangle$ values ranging from 0.1° to 0.6°. When combined with the results from the 1.2 m tall slip face of *Sutton et al.* [2013a, 2013b], in which $\langle\theta_c\rangle$ and $\langle\theta_c\rangle - \langle\theta_r\rangle$ had values of 34° and 2°, respectively, the available data suggest that $\langle\theta_c\rangle$ and $\langle\theta_c\rangle - \langle\theta_r\rangle$ both vary inversely with slip-face height.

Our observation that the mean critical angle decreases slightly with increasing dune size needs further study and verification given the prevailing wisdom that the critical slope is independent of system size in a slope of identical grains. However, we wish to stress that this finding does not necessarily imply that the angle of friction depends on system size. The critical angle is equal to the angle of friction only if a Mohr-Coulomb failure criterion is assumed. In the Drucker-Prager criterion [Drucker and Prager, 1952], widely used in soil physics (including for cohesionless materials), the critical angle can exceed the friction angle [Modaressi and Evesque, 2001]. Also, it is possible that the angle of friction depends (slightly) on the system size, perhaps as a consequence of the natural variability in compaction and/or grain shape. A dune slip face or sandpile is a disordered system because local static friction angles take on a range of values [e.g., Zhou and Ooi, 2009] due to local variations in compaction and grain roundedness [e.g., Bareither et al., 2008], with the consequence that contact forces exhibit long-range correlation [Majmudar and Behringer, 2005; Ostojic et al., 2006]. A distribution of static friction angles may give rise to system-size dependence of the critical angle because this angle is controlled by the static friction angle of the weakest patch within the zone of grain-fall deposition (i.e., the one with the lowest static friction angle). Large dunes are likely to have more weak zones compared to small dunes because they include more samples from the distribution of static friction angles (hence more values on the low-friction-angle tail of the distribution) compared to small dunes.

5. Conclusions

Our conclusions can be summarized as follows:

1. The mean critical angle varies inversely with wind speed or shear velocity. Available data and 3-D LES modeling results are consistent with the hypothesis that variations in $\langle\theta_c\rangle$ are primarily the result of changes in the magnitude of turbulent shear stresses that randomly act in the downslope direction (i.e., in the direction of gravity) triggering failure at lower angles than would otherwise be possible.
2. The frequency of avalanching is driven by two components: the standard accommodation-space-filling component proportional to sediment flux coming over the brinkline and a new, previously undocumented, rotational component related to the change in the mean critical angle with time, which, in turn, is related to the increase in the magnitude of turbulent shear stresses with increasing wind speeds. In our study site the rotational component has the effect of causing the frequency of avalanching to reach a maximum value earlier in the day than the maximum in sediment flux.
3. The mean critical angle has an inverse relationship with slip-face height. Specifically, under dry-sand conditions the 30 m tall slip face had $\langle\theta_c\rangle = 32.2^\circ\text{--}32.35^\circ$ and the 17 m tall slip face had $\langle\theta_c\rangle = 32.2^\circ\text{--}33^\circ$, with larger values (and hence larger differences) associated with slower winds. Combining these data with the $\langle\theta_c\rangle$ value of 34° from the 1.2 m tall slip face of the *Sutton et al.* [2013a, 2013b], available data suggest that $\langle\theta_c\rangle$ varies inversely with slip-face height, although this relationship must be valid only to some limit.

4. The relaxation angle also has an inverse relationship with slip-face height, reflecting an inverse relationship of the critical angle with height but no such relationship for the angle of repose. The 30 m tall slip face had a $\langle\theta_c\rangle - \langle\theta_r\rangle$ value of $\approx 0.1^\circ$, the 17 m tall slip-face had $\langle\theta_c\rangle - \langle\theta_r\rangle$ values in the range of 0.2° – 0.8° , and the 1.2 m tall slip face of Sutton *et al.* [2013a, 2013b] had a $\langle\theta_c\rangle - \langle\theta_r\rangle$ value of $\approx 2^\circ$. These data suggest that the relaxation angle varies inversely with slip-face height.
5. The mean critical angle depends sensitively on the moisture of the sand. While this is not a new result, the measurement of this effect using TLS is new and the moisture effects we measured are dramatic: even a modest input of moisture (e.g., one half hour of low-intensity rainfall yielding 1% sand moisture) can result in a 1–2 order-of-magnitude decrease in the frequency of avalanching that can persist for days.

Acknowledgments

This work was partially supported by NSF grants to Ellis (1063441) and Sherman (1340644). We thank Ryan Ewing and Doug Jerolmack for their helpful suggestions and A.E. Michel Louge and three anonymous reviewers for their help in strengthening the paper. Any data can be obtained upon request from J.D.P.

References

- Allen, J. (1970), The avalanching of granular solids on dune and similar slopes, *J. Geol.*, *78*, 326–351, doi:10.1086/627520.
- Anderson, R. S. (1988), The pattern of rainfall deposition in the lee of aeolian dunes, *Sedimentology*, *35*(2), 175–188, doi:10.1111/j.1365-3091.1988.tb00943.x.
- Andreotti, B., P. Claudin, and S. Douady (2002), Selection of dune shapes and velocities, Part 2: A two-dimensional modeling, *Eur. Phys. J. B*, *28*, 341–352, doi:10.1140/epjb/e2002-00237-3.
- Baas, A. C. W., and J. M. Niell (2007), Modelling vegetated dune landscapes, *Geophys. Res. Lett.*, *34*, L06405, doi:10.1029/2006GL029152.
- Bagnold, R. A. (1941), *The Physics of Blown Sand and Desert Dunes*, 265 pp., Methuen, London.
- Bagnold, R. A. (1966), The shearing and dilatation of dry sand and the 'singing' mechanism, *Proc. R. Soc. London A*, *295*(1442), 219–232, doi:10.1098/rspa.1966.0236.
- Bareither, C. A., T. B. Edil, C. H. Benson, and D. M. Mickelson (2008), Geological and physical factors affecting the friction angle of compacted sands, *J. Geotech. Geoenviron. Eng.*, *134*(10), 1476–1489, doi:10.1061/(ASCE)1090-0241(2008)134:10(1476).
- Bauer, B. O., and R. G. Davidson-Arnott (2003), A general framework for modeling sediment supply to coastal dunes including wind angle, beach geometry, and fetch effects, *Geomorphology*, *49*(1), 89–108, doi:10.1016/S0169-555X(02)00165-4.
- Bo, T.-L., and X.-J. Zheng (2013), Wind speed-up process on the windward slope of dunes in dune fields, *Comput. Fluids*, *71*, 400–405, doi:10.1016/j.compfluid.2012.11.007.
- Börzsönyi, T., T. C. Halsey, and R. E. Ecke (2008), Avalanche dynamics on a rough inclined plane, *Phys. Rev. E*, *78*, 011306, doi:10.1103/PhysRevE.78.011306.
- Bourke, M. C. (2010), Barchan dune asymmetry: Observations from Mars and Earth, *Icarus*, *205*(1), 183–197, doi:10.1016/j.icarus.2009.08.023.
- Bourke, M. C., K. S. Edgett, and B. A. Cantor (2008), Recent aeolian dune change on Mars, *Geomorphology*, *94*, 247–255.
- Breton, C., N. Lancaster, and W. G. Nickling (2008), Magnitude and frequency of grain flows on a desert sand dune, *Geomorphology*, *95*(3–4), 518–523, doi:10.1016/j.geomorph.2007.07.004.
- Brown, R. L., and J. C. Richards (1966), *Principles of Powder Mechanics*, 246 pp., Pergamon Press, Oxford, U. K.
- Choi, H., and P. Moin (2012), Grid-point requirements for large eddy simulation: Chapman's estimates revisited, *Phys. Fluids*, *24*, 011702, doi:10.1063/1.3676783.
- Chu, C. R., M. B. Parlange, G. G. Katul, and J. D. Albertson (1996), Probability density functions of turbulent velocity and temperature in the atmospheric surface layer, *Water Resour. Res.*, *32*, 1681–1688, doi:10.1029/96WR00287.
- Claudin, P., and B. Andreotti (2006), A scaling law for aeolian dunes on Mars, Venus, Earth, and for subaqueous ripples, *Earth Planet. Sci. Lett.*, *252*, 30–44, doi:10.1016/j.epsl.2006.09.004.
- Dai, A., and C. Deser (1999), Diurnal and semi-diurnal variations in global surface wind and divergence fields, *J. Geophys. Res.*, *104*, 31,109–31,125, doi:10.1029/1999JD900927.
- Drucker, D. C., and W. Prager (1952), Soil mechanics and plastic analysis for limit design, *Q. Appl. Math.*, *10*(2), 157–165.
- Duran, J. (2000), *Sands, Powders, and Grains: An Introduction to the Physics of Granular Materials*, 227 pp., Springer, New York.
- Elbelhiti, H., P. Claudin, and B. Andreotti (2005), Field evidence for surface-wave-induced instability of sand dunes, *Nature*, *437*, 720–723.
- Ellis, J. T., D. J. Sherman, E. J. Farrell, and B. Li (2012), Temporal and spatial variability of aeolian sand transport: Implications for field measurements, *Aeolian Res.*, *3*, 379–387, doi:10.1016/j.aeolia.2011.06.001.
- Exner, F. M. (1925), Über die wechselwirkung zwischen wasser und geschiebe in flüssen, *Akad. Wiss. Wien Math. Naturwiss. Kl.*, *134*(2a), 165–204.
- Farrell, E. J., D. J. Sherman, J. Ellis, and B. Li (2012), Vertical distribution of grain size for wind blown sand, *Aeolian Res.*, *7*, 51–61, doi:10.1016/j.aeolia.2012.03.003.
- Fischer, S., M. E. Cates, and K. Kroy (2008), Dynamic scaling of desert dunes, *Phys. Rev. E*, *77*, 031302.
- Gipprich, T. L., R. K. Snieder, R. W. Jibson, and W. Kimman (2008), The role of shear and tensile failure in dynamically triggered landslides, *Geophys. J. Int.*, *172*, 770–778, doi:10.1111/j.1365-246X.2007.03681.x.
- Herrmann, H. J., J. S. Andrade, V. Schatz, G. Sauermann, and E. J. R. Parteli (2005), Calculation of the separation streamlines of barchans and transverse dunes, *Physica A*, *357*(1), 44–49, doi:10.1016/j.physa.2005.05.057.
- Hersen, P., S. Douady, and B. Andreotti (2002), Relevant length scale for barchan dune, *Phys. Rev. Lett.*, *89*, 264301.
- Hesp, P. A. (2004), Coastal dunes in the tropics and temperate regions: Location, formation, morphology and vegetation processes, in *Coastal Dunes, Ecology and Conservation*, edited by M. L. Martinez, and N. P. Psuty, pp. 29–49, Springer, Berlin, doi:10.1007/978-3-540-74002-5_3.
- Hesp, P. A., and K. Hastings (1998), Width, height and slope relationships and aerodynamic maintenance of barchans, *Geomorphology*, *22*(2), 193–204.
- Hirt, C. W., and B. D. Nicholas (1981), Volume of fluid (vof) method for the dynamics of free boundaries, *J. Comput. Phys.*, *39*, 201–225.
- Hodge, R., J. Brasington, and K. Richards (2009), In situ characterization of grain-scale fluvial morphology using Terrestrial Laser Scanning, *Earth Surf. Processes Landforms*, *34*, 954–968, doi:10.1002/esp.1780.
- Horgan, B., and J. Bell (2012), Active slipface avalanches in the north polar sand sea of Mars: Evidence for a wind-related origin, *Geophys. Res. Lett.*, *39*, L09201, doi:10.1029/2012GL051329.
- Howard, A. D. (1977), Effect of slope on the threshold of motion and its application to orientation of wind ripples, *Geol. Soc. Am. Bull.*, *88*, 853–856, doi:10.1130/0016-7606(1977)88<853:EOSOTT>2.0.CO;2.

- Huang, J., and D. L. Turcotte (1990), Are earthquakes an example of deterministic chaos?, *Geophys. Res. Lett.*, *17*, 223–226, doi:10.1029/GL017i003p00223.
- Hunter, R. E. (1977), Basic types of stratification in small eolian dunes, *Sedimentology*, *24*, 361–387, doi:10.1111/j.1365-3091.1977.tb00128.x.
- Hunter, R. E. (1985), A kinematic model for the structure of lee-side deposits, *Sedimentology*, *32*(3), 409–422, doi:10.1111/j.1365-3091.1985.tb00520.x.
- Iversen, J. D., and K. R. Rasmussen (1999), The effect of wind speed and bed slope on sand transport, *Sedimentology*, *46*, 723–731, doi:10.1046/j.1365-3091.1999.00245.x.
- Jerolmack, D. J. (2008), Rice piles and sticky deltas: Sediment transport fluctuations in threshold-dominated systems, Abstract #H52C-08 presented at 2008 AGU Fall Meeting.
- Jerolmack, D. J., and C. Paola (2010), Shredding of environmental signals by sediment transport, *Geophys. Res. Lett.*, *37*, L19401, doi:10.1029/2010GL044638.
- Jimenez, J. A., L. P. Maia, J. Serra, and J. Morais (1999), Aeolian dune migration along the Ceará coast, northeastern Brazil, *Sedimentology*, *46*, 689–701, doi:10.1046/j.1365-3091.1999.00240.x.
- Jop, P., Y. Forterre, and O. Pouliquen (2006), A constitutive law for dense granular flows, *Nature*, *441*, 727–730, doi:10.1038/nature04801.
- Katsuki, A., M. Kikuchi, H. Nishimori, N. Endo, and K. Taniguchi (2011), Cellular model for sand dunes with saltation, avalanche and strong erosion: Collisional simulation of barchans, *Earth Surf. Processes Landforms*, *36*(3), 372–382.
- Kocurek, G., and R. H. Dott Jr. (1981), Distinctions and uses of stratification types in the interpretation of eolian sand, *J. Sediment. Res.*, *51*(2), 579–595, doi:10.1306/212F7CE3-2B24-11D7-8648000102C1865D.
- Lancaster, N., W. G. Nickling, C. K. McKenna Neuman, and V. E. Wyatt (1996), Sediment flux and airflow on the stoss slope of a barchan dune, *Geomorphology*, *17*, 55–62.
- Levin, N., H. Tsoar, H. J. Herrmann, L. P. Maia, and V. Claudino-Sales (2009), Modelling the formation of residual dune ridges behind barchan dunes in North-east Brazil, *Sedimentology*, *56*(6), 1623–1641, doi:10.1111/j.1365-3091.2009.01048.x.
- Li, B., D. J. Sherman, E. J. Farrell, and J. T. Ellis (2010), Variability of the apparent von Kármán parameter during aeolian saltation, *Geophys. Res. Lett.*, *37*, L15404, doi:10.1029/2010GL044068.
- Li, B., J. T. Ellis, and D. J. Sherman (2014), Estimating the impact threshold for wind-blown sand, *J. Coastal Res.*, *70*, 627–632.
- Maia, L. P., G. S. S. Freire, and L. D. Lacerda (2005), Accelerated dune migration and aeolian transport during El Niño events along the NE Brazilian Coast, *J. Coastal Res.*, *21*(6), 1121–1126, doi:10.2112/03-702A.1.
- Majmudar, T. S., and R. P. Behringer (2005), Contact force measurements and stress-induced anisotropy in granular materials, *Nature*, *435*, 1079–1082, doi:10.1038/nature03805.
- McDonald, R. R., and R. S. Anderson (1996), Constraints on eolian grain flow dynamics through laboratory experiments on sand slopes, *J. Sediment. Res.*, *66*, 642–653, doi:10.1306/D42683D3-2B26-11D7-8648000102C1865D.
- Modaresi, A., and P. Evesque (2001), Is the friction angle the maximum slope of a free surface of a cohesionless material?, *Poudres Grains*, *12*(5), 83–102.
- Nickling, W. G., C. M. Neuman, and N. Lancaster (2002), Grainfall processes in the lee of transverse dunes, Silver Peak, Nevada, *Sedimentology*, *49*, 191–209, doi:10.1046/j.1365-3091.2002.00443.x.
- Omidyeganeh, M., U. Piomelli, K. T. Christensen, and J. L. Best (2013), Large eddy simulation of interacting barchan dunes in a steady, unidirectional flow, *J. Geophys. Res. Earth Surf.*, *118*, 2089–2104, doi:10.1002/jgrf.20149.
- Ostojic, S., E. Somfai, and B. Nienhuis (2006), Scale invariance and universality of force networks in static granular matter, *Nature*, *439*, 828–830, doi:10.1038/nature04549.
- Parteli, E. J., O. Duran, and H. J. Herrmann (2007), Minimal size of a barchan dune, *Phys. Rev. E*, *75*(1), 011301, doi:10.1103/PhysRevE.75.011301.
- Pelletier, J. D. (2000), Spring-block models of seismicity: Review and analysis of a structurally-heterogeneous model coupled to a viscous asthenosphere, in *Geocomplexity and the Physics of Earthquakes*, *Geophys. Monogr. Ser.*, vol. 120, pp. 27–42, AGU, Washington, D. C., doi:10.1029/GM120p0027.
- Pelletier, J. D. (2009), Controls on the height and spacing of eolian ripples and transverse dunes: A numerical modeling investigation, *Geomorphology*, *105*, 322–333, doi:10.1016/j.geomorph.2008.10.010.
- Quartier, L., B. Andreotti, S. Douady, and A. Daerr (2000), Dynamics of a grain on a sandpile model, *Phys. Rev. E*, *62*(6), 8299–8307, doi:10.1103/PhysRevE.62.8299.
- Reitz, M. D., and D. J. Jerolmack (2012), Experimental alluvial fan evolution: Channel dynamics, slope controls, and shoreline growth, *J. Geophys. Res.*, *117*, F02021, doi:10.1029/2011JF002261.
- Robinson, D., and S. Friedman (2002), Observations of the effects of particle shape and particle size distribution on avalanching of granular media, *Physica A*, *311*(1–2), 97–110, doi:10.1016/S0378-4371(02)00815-4.
- Sauermann, G., J. S. Andrade Jr., L. P. Maia, U. M. S. Costa, A. D. Araújo, and H. J. Herrmann (2003), Wind velocity and sand transport on a barchan dune, *Geomorphology*, *54*(3), 245–255, doi:10.1016/S0169-555X(02)00359-8.
- Shao, Y. (2008), *Physics and Modelling of Wind Erosion*, 2nd ed., 452 pp., Springer, Berlin.
- Sherman, D. J. (1992), An equilibrium relationship for shear velocity and apparent roughness length in aeolian saltation, *Geomorphology*, *5*, 419–431, doi:10.1016/0169-555X(92)90016-H.
- Sherman, D. J., and E. J. Farrell (2008), Aerodynamic roughness length over movable beds: Comparison of wind tunnel and field data, *J. Geophys. Res.*, *113*, F02S08, doi:10.1029/2007JF000784.
- Sherman, D. J., C. Houser, J. T. Ellis, E. J. Farrell, B. Li, and L. P. Maia (2013a), Characterization of aeolian streamers using time-average videography, *J. Coastal Res.*, *65*, 1331–1336.
- Sherman, D. J., B. Li, J. T. Ellis, E. J. Farrell, L. P. Maia, and H. Granja (2013b), Recalibrating aeolian sand transport models, *Earth Surf. Processes Landforms*, *38*, 169–178, doi:10.1002/esp.3310.
- Sherman, D. J., C. Swann, and J. D. Barron (2014), A high-efficiency, low-cost aeolian sand trap, *Aeolian Res.*, *13*, 31–34, doi:10.1016/j.aeolia.2014.02.006.
- Stout, J. E. (2010), Diurnal patterns of blowing sand, *Earth Surf. Processes Landforms*, *35*(3), 314–318, doi:10.1002/esp.1919.
- Sutton, S. L. F., C. McKenna Neuman, and W. Nickling (2013a), Lee slope sediment processes leading to avalanche initiation on an aeolian dune, *J. Geophys. Res. Earth Surf.*, *118*, 1754–1766, doi:10.1002/jgrf.20131.
- Sutton, S. L. F., C. McKenna Neuman, and W. Nickling (2013b), Avalanche grainflow on a simulated aeolian dune, *J. Geophys. Res. Earth Surf.*, *118*, 1767–1776, doi:10.1002/jgrf.20130.
- Walker, I., and W. Nickling (2002), Dynamics of secondary airflow and sediment transport over and in the lee of transverse dunes, *Prog. Phys. Geogr.*, *26*(1), 47–75, doi:10.1191/0309133302pp325ra.
- Warren, A. (2013), *Dunes: Dynamics, Morphology, History*, 219 pp., Wiley-Blackwell, New York.

- Werner, B. T. (1995), Eolian dunes: Computer simulations and attractor interpretation, *Geology*, 23, 1107–1110, doi:10.1130/0091-7613(1995)023<1107:EDCSAA>2.3.CO;2.
- Wheaton, J. M., J. Brasington, S. E. Darby, and D. A. Sear (2010), Accounting for uncertainty in DEMs from repeat topographic surveys: Improved sediment budgets, *Earth Surf. Processes Landforms*, 35(2), 136–156, doi:10.1002/esp.1886.
- Wiggs, G. F. S., I. Livingstone, and A. Warren (1996), The role of streamline curvature in sand dune dynamics: Evidence from field and wind tunnel measurements, *Geomorphology*, 17, 29–46.
- Wu, X., X. Zou, Z. C. Zheng, and C. Zhang (2011), Field measurement and scaled-down wind-tunnel model measurement of airflow field over a barchan dune, *J. Arid Environ.*, 75(5), 438–445, doi:10.1016/j.jaridenv.2010.12.016.
- Yang, H., R. Li, P. Kong, Q. C. Sun, M. J. Biggs, and V. Zivkovic (2015), The dynamics of granular materials under the slumping regime in a rotating drum as revealed by speckle visibility spectroscopy, *Phys. Rev. E*, 91, 042206, doi:10.1103/PhysRevE.91.042206.
- Zhang, D., C. Narteau, and O. Rozier (2010), Morphodynamics of barchan and transverse dunes using a cellular automaton model, *J. Geophys. Res.*, 115, F03041, doi:10.1029/2009JF001620.
- Zhang, D., X. Yang, O. Rozier, and C. Narteau (2014), Mean sediment residence time in barchan dunes, *J. Geophys. Res. Earth Surf.*, 119, 451–463, doi:10.1002/2013JF002833.
- Zhou, C., and J. Y. Ooi (2009), Numerical investigation of progressive development of granular pile with spherical and non-spherical particles, *Mech. Mater.*, 41, 707–714, doi:10.1016/j.mechmat.2009.01.017.